Precise and accurate determination of the ^{8}B decay spectrum

O. S. Kirsebom,[1,*] S. Hyldegaard,[1] M. Alcorta,[2,†] M. J. G. Borge,[2] J. Büscher,[3] T. Eronen,[4] S. Fox,[5] B. R. Fulton,[5] H. O. U. Fynbo,[1] H. Hultgren,[6] A. Jokinen,[4] B. Jonson,[6] A. Kankainen,[4] P. Karvonen,[4] T. Kessler,[4,‡] A. Laird,[5] M. Madurga,[2,§] I. Moore,[4] G. Nyman,[6] H. Penttilä,[4] S. Rahaman,[4,‖] M. Reponen,[4] K. Riisager,[1] T. Roger,[3] J. Ronkainen,[4,¶] A. Saastamoinen,[4] O. Tengblad,[2] and J. Äystö[4]

[1]*Department of Physics and Astronomy, Aarhus University, DK-8000 Aarhus C, Denmark*
[2]*Instituto de Estructura de la Materia, CSIC, Serrano 113 bis, E-28006 Madrid, Spain*
[3]*Instituut voor Kern-en Stralingsfysica, Katholieke Universiteit Leuven, B-3001 Leuven, Belgium*
[4]*Department of Physics, University of Jyväskylä, FIN-40351 Jyväskylä, Finland*
[5]*Department of Physics, University of York, York YO10 5DD, United Kingdom*
[6]*Fundamental Physics, Chalmers University of Technology, S-41296 Göteborg, Sweden*

(Received 14 April 2011; published 6 June 2011)

Accurate measurements of the ^{8}B neutrino spectrum are important for the interpretation of solar neutrino data. Experimentally, the ^{8}B neutrino spectrum can be obtained from the measurement of the β-delayed α spectrum. We report on an α-α coincidence measurement performed at the IGISOL facility in Jyväskylä, Finland. Our measurement allows extensive cross-checks to be performed and gives a more intense neutrino spectrum at high energies compared to the present standard. The deviation reaches 4% at the end point of the spectrum. Below 11 MeV, the deviation is less than 1%.

DOI: 10.1103/PhysRevC.83.065802 PACS number(s): 26.65.+t, 23.40.−s, 27.20.+n

I. INTRODUCTION

The neutrinos from the β decay of ^{8}B constitute only a small fraction of the total solar neutrino flux [1], yet they play a central role in the interpretation of solar neutrino measurements owing to their high energies, reaching up to 17 MeV. Apart from the tiny contribution made by the *hep* neutrinos from the $^3\mathrm{He} + p \rightarrow {}^4\mathrm{He} + e^+ + \nu_e$ reaction, ^{8}B provides the only source of solar neutrinos above 2 MeV and hence the only source of detectable solar neutrinos for the neutrino detectors Super-Kamiokande (SK) and Sudbury Neutrino Observatory (SNO), which both have a detection threshold of 4 MeV.

Before conclusive experimental evidence for the large mixing angle Mikheev-Smirnov-Wolfenstein (MSW) solution [2–4] to the solar neutrino problem was provided by SNO [5], attempts were made [6] to discriminate between the various proposed solutions using, among other observables, the shape of the solar neutrino energy spectrum measured by SK. More recently, the solar neutrino energy spectra measured by SK and SNO have been analyzed [7,8] with the aim to study the spectral distortion expected owing to the transition from vacuum oscillations below 3 MeV to matter-enhanced oscillations above 3 MeV. No sign of distortion was found at the level of sensitivity of the analyses. Above the detection thresholds of SK and SNO, the distortion is expected to be on the order of 10%. Within a decade, SK should be able to resolve a 10% distortion with 3σ significance [9]. Searches for a *hep* neutrino signal have been made by analyzing the high-energy end of the solar neutrino spectrum, but so far only an upper limit has been placed on the *hep* neutrino flux [10]. The above analyses all require accurate knowledge of the *un*distorted solar neutrino spectrum. Uncertainties on the undistorted spectrum complicate the search for spectral distortion and may obscure a possible *hep* neutrino signal.

With the advent of new solar neutrino detectors such as KamLAND and Borexino, the measurements of the solar neutrino spectrum are being extended to lower energies. Accurate knowledge of the ^{8}B neutrino spectrum plays an important role in these continued efforts to improve our understanding of neutrinos. Recently, Borexino was able to confirm [11] the enhancement of the oscillation probability above 3 MeV owing to the transition from vacuum to matter-enhanced oscillations. Their result relied not so much on the shape of the ^{8}B neutrino spectrum as on the relative intensities of the ^{8}B and ^{7}Be neutrinos.

The β decay of ^{8}B populates a broad range of excitation energies in ^{8}Be. Subsequently, the excited ^{8}Be nucleus breaks up into two α particles, as illustrated schematically in Fig. 1. Transitions from the 2^+ ground state of ^{8}B to the 0^+ ground state of ^{8}Be or the very broad 4^+ state at 11.4 MeV are second forbidden and hence strongly suppressed. A recent experimental study [13] gives an upper limit of 7.3×10^{-5} for the branching ratio to the ground state. No 1^+ or 3^+ states in ^{8}Be are energetically accessible in β decay (though the 1^+, $T = 1$ state at 17.640 MeV is energetically accessible in electron-capture decay). This means that the decay proceeds exclusively by allowed transitions to the 2^+ states. The

*Corresponding author: oliskir@phys.au.dk; present address: TRIUMF, Vancouver, BC, Canada V6T 2A3.
†Present address: Physics Division, Argonne National Laboratory, Argonne, IL 60439, USA.
‡Present address: Division Optics, Physikalisch-Technische Bundesanstalt, Bundesallee 100, D-38116 Braunschweig, Germany.
§Present address: Department of Physics and Astronomy, University of Tennessee, Knoxville, TN 37996, USA.
‖Present address: Physics Division, P-23, Mail Stop H803, Los Alamos National Laboratory, Los Alamos, NM 87545, USA.
¶Present address: Nokia, Tampere, Finland.

 ©2011 American Physical Society

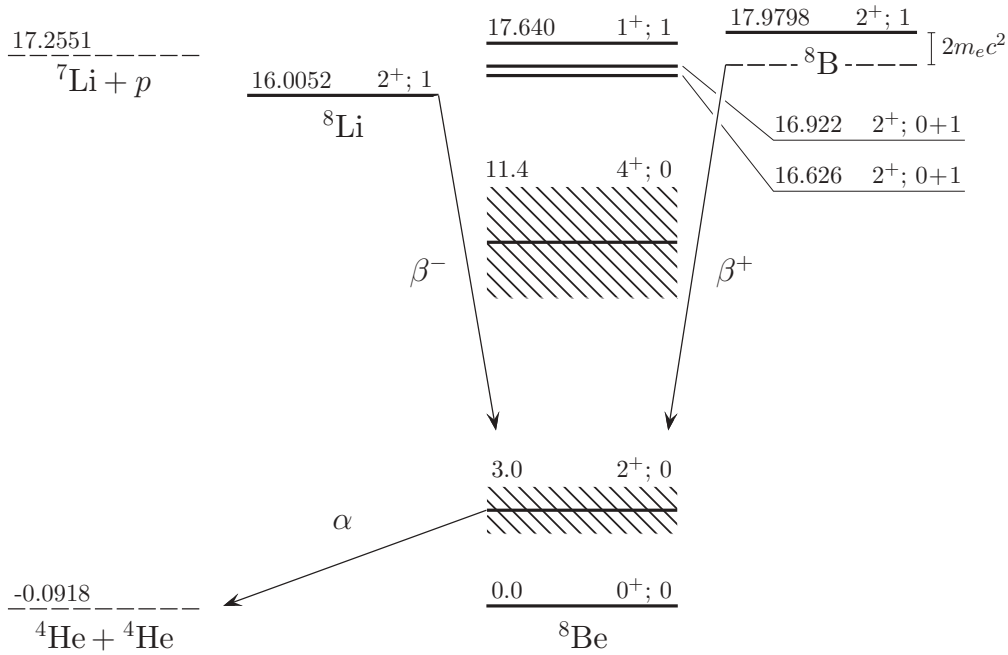

FIG. 1. Nuclear levels in the $A = 8$ isospin triplet below the ground state of ^{8}B. The levels are labeled by their energy above the ^{8}Be ground state in MeV, their spin-parity, and their isospin. Energies and quantum numbers are taken from Ref. [12]. The 16.626- and 16.922-MeV states are strongly isospin mixed.

majority of the decays proceed via the broad 3-MeV state, resulting in a broad distribution of α-particle energies peaked around 1.5 MeV. Henceforth, the distribution of excitation energies populated in ^{8}Be is referred to as the E_x distribution. Measurement of either the β energy or the α energies provides experimental determination of the E_x distribution from which the neutrino spectrum can be calculated.

In the first studies [14–16] of the β decay of ^{8}B, only singles α spectra were measured, and the E_x distribution had to be unfolded from the recoil-broadening distribution. The singles β spectrum has been measured by Ref. [17]. In this case, the E_x distribution had to be unfolded from an even broader β spectrum.

A measurement of the total energy of the two α particles provides a direct (no need for unfolding) and hence more reliable determination of the E_x distribution. Such measurements have only recently become feasible thanks to advances in detector technology. In the first measurement of this type [18] performed at Notre Dame, the ^{8}B activity was implanted in a thin carbon foil, and the α particles were measured in coincidence in two Si detectors placed at opposite sides of the foil. A strong magnetic field was applied to sweep away the positrons. In this way, β summing and unwanted β-α coincidences were effectively eliminated. In the second measurement of this type [19], performed at Argonne, the ^{8}B activity was implanted in a Si detector and the total energy of the α particles directly measured. One great advantage of this approach is the complete absence of insensitive layers of material in which the α particles lose energy. One drawback is the systematic shift in energy of several tens of keV owing to β summing that must be accounted for with simulations. In between the Notre Dame and Argonne measurements, another measurement was performed at the University of Washington in Seattle [20] using a conventional single-α technique. The Argonne and Seattle measurements are in excellent agreement but disagree with the Notre Dame measurement. The E_x distribution deduced from the Notre Dame data is slightly wider and the peak of the distribution is shifted 50 keV down in energy with respect to the Argonne and Seattle distributions. The uncertainties on the peak position are 12 keV (Notre Dame), 9 keV (Argonne), and 6 keV (Seattle).

This disagreement provided the motivation for our measurement, though recently it was reported [21] that the members of the Notre Dame collaboration now recognize that they underestimated uncertainties related to the energy loss generated by the carbon buildup in their foil, so a claim of a disagreement between their measurement and the Argonne and Seattle measurements no longer should be made. We have performed two independent experiments in which the energy of the two α particles was measured by different techniques. The first experiment was performed at the IGISOL facility in Jyväskylä, Finland, using a coincidence technique similar to that used at Notre Dame. The second experiment was performed at the KVI facility in Groningen, The Netherlands, using an implantation technique similar to that used at Argonne. In both cases, a careful investigation of the response of the detection system was necessary to obtain the desired accuracy of 5–10 keV. Special attention had to be paid to the energy calibration, which was the main source of uncertainty in the previous studies.

In this article we present the results of the IGISOL experiment. A second article devoted to the KVI experiment is under preparation [22]. A third article describing the calculation of the neutrino spectrum from the measured E_x

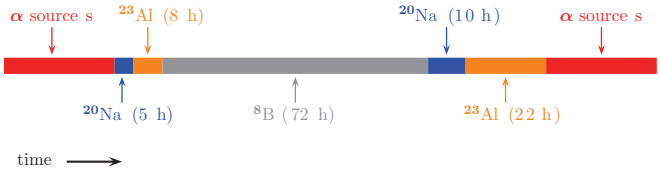

FIG. 2. (Color online) Time line of the measurement program.

distribution is planned. The present article is structured as follows: Section II describes the present experimental setup. Section III gives a detailed account of the calibration procedure and associated systematical uncertainties. Its subsections, each dealing with their own aspect of the detection system, can to a large extent be read independently of one another. Section IV discusses the kinematics and correlations in the β decay of ^{8}B and describes the implementation of a Monte Carlo simulation to determine the α-α coincidence detection efficiency of the setup. Section V is concerned with the analysis of the experimental data. Section VI discusses the R-matrix parameterization of the data. The E_x distribution obtained from the present study is compared to the distributions obtained in previous studies, and the implications for the neutrino spectrum are discussed. Finally, Sec. VII summarizes and concludes. The reader who is interested in physics discussion and results but not in careful analysis of experimental effects, may want to skip Sec. III and IV.

II. EXPERIMENTAL PROCEDURE

The measurement program is shown in Fig. 2. Calibration measurements were made both at the beginning and at the end of the experiment, using the radioactive isotopes ^{20}Na and ^{23}Al produced online as well as standard α sources. From the beginning of the first ^{20}Na run to the end of the second ^{23}Al run, the vacuum of the experimental chamber was never broken.

A. Radioactive beam production

The radioactive beams were produced with the IGISOL technique [23], using a light-ion fusion ion guide [24] and p and ^{3}He primary beams from the K130 cyclotron of the Accelerator Laboratory of University of Jyväskylä. With the IGISOL technique, a fraction of the reaction products are slowed down and thermalized in a buffer gas whereby the charge state typically is reduced to $q = 1^+$. For the present experiment, helium was used at a pressure of 300 mbar. The thermalized ions are transported toward the separator by a continuous flow of gas and by electric fields through a differentially pumped vacuum system and a sextupole ion guide electrode structure [25]. Upon injection into the high-vacuum section of the separator, the ions are first accelerated and then separated according to their mass-to-charge ratio (A/q) using a 55° dipole magnet with typical mass resolving power of $M/\Delta M = 500$.

The ^{8}B beam was produced through the ^{6}Li(^{3}He, n)^{8}B reaction. The target consisted of 1.95 mg/cm^2 LiF with 95% enriched ^{6}Li, evaporated on a 3.2 mg/cm^2 Al backing. During the first 24 h of ^{8}B production, the energy of the ^{3}He beam was 15 MeV. Before striking the LiF target, the ^{3}He beam had to pass through a 4.5 mg/cm^2 Havar window (cyclotron collimator) and a 25.6 mg/cm^2 Ni foil (ion guide gas window), whereby the energy was reduced to 7.0 MeV with an estimated 1σ spread of 0.3 MeV. After the first 24 h of ^{8}B production, the energy of the ^{3}He beam was lowered to 14 MeV, resulting in an energy of 5.2 MeV on target, to exploit the fact that the ^{6}Li(^{3}He, n) cross section peaks at 5 MeV [26]. The acceleration voltage was 20 kV, resulting in the ^{8}B ions, on average, being implanted midway into a carbon foil of thickness 26 μg/cm^2. The average implantation rate during 72 h of measurement was 200 ions per second with a typical ^{3}He beam intensity of 0.3 μA. At the end of the experiment, the beam spot on the carbon foil was clearly visible. Its diameter was measured to be 7 mm.

By choosing the beam energy on target to be 7.0 MeV (later 5.2 MeV), we ensured that no ^{8}Li was produced through the ^{7}Li(^{3}He, $2p$)^{8}Li reaction which has a threshold of 8.1 MeV. The presence of ^{8}Li activity in the mass separated beam would constitute a very serious problem. To our setup, the β^- decay of ^{8}Li is essentially indistinguishable from the β^+ decay of ^{8}B. For 2 h, the primary beam was operated in pulsed mode (on for 2 s, then off for 6 s). The β trigger rate was used to monitor the increase in activity during the 2-s beam-on period and the exponential decline in activity during the 6-s beam-off period. A half-life of 766^{+6}_{-16} ms was deduced from these measurements, in good agreement with the ^{8}B literature value of 770 ± 3 ms [12]. The inclusion of a ^{8}Li component in the fit function with the half-life fixed to 840.3 ms [27] gave an upper limit of $\sim 10^{-5}$ on the ^{8}Li fraction. The small difference between the half-lives of ^{8}B and ^{8}Li makes it difficult to put better limits on the ^{8}Li fraction.

The beams used for calibration, ^{20}Na and ^{23}Al, were produced through the reactions ^{24}Mg(p, $n\alpha$)^{20}Na and ^{24}Mg(p, $2n$)^{23}Al, respectively. The beam energy was 40 MeV with a typical intensity of 8–10 μA, and the target was self-supporting 4.3 mg/cm^2 natural Mg. The average ^{20}Na implantation rate was 2×10^4 ions per second. The average ^{23}Al implantation rate was 2×10^2 per second, though the total $A = 23$ implantation rate was much higher, 5×10^4 per second, because the mass separated $A = 23$ beam contains vast amounts of ^{23}Mg produced through the ^{24}Mg(p, pn)^{23}Mg reaction. The present Al-to-Mg ratio is consistent with the ratio of 1:200 reported in Ref. [28].

B. Detection system

The detection system consisted of four 60-μm-thick, double-sided silicon strip detectors (DSSSD), each backed by a 1.5-mm-thick, unsegmented silicon detector. The detectors were placed 5 cm from the carbon foil in a rectangular configuration as shown in Fig. 3, whereby a solid-angle coverage of 30% was achieved with an angular resolution of 3°. The carbon foil was perpendicular to the beam.

The thickness of the DSSSDs is such that the most energetic α particles (~8.5 MeV) are completely stopped. The unsegmented Si detectors placed behind the DSSSDs serve

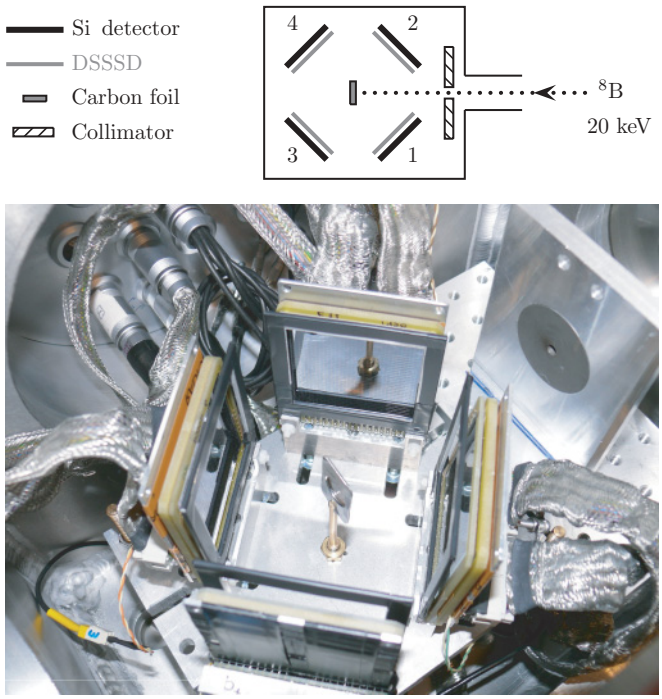

FIG. 3. (Color online) Schematic and simplified illustration of the experimental setup (top view) and picture of the experimental setup: Four DSSSDs backed by unsegmented Si detectors surrounding the carbon foil in the center. The beam comes in from the right through the 5-mm collimator.

to detect β particles. The DSSSDs measure 5×5 cm^2, and both sides are divided into 16 strips running in perpendicular directions. The front side is p^+ doped; the back side n^+ doped. The p^+-doped layer on the front side is only 100 nm deep. An aluminum grid, forming the front contact of the detector, covers 4% of the active surface. Further details regarding the design and performance of the DSSSDs are given in Ref. [29]. A feature that deserves to be emphasized is the very thin dead layer of only 100 nm (over 96% of the active surface) which facilitates the detection of low-energy ions. In Ref. [29] it is stated, wrongly, that the aluminum grid covers 2% of the active surface. The correct number is the one given here, that is, 4%.

The $4 \times 2 \times 16 = 128$ channels from the DSSSDs were read out using eight 16-channel preamplifiers and fed to eight 16-channel amplifiers distributing energy and time signals to the analog-to-digital converter (ADC) and time-to-digital converter (TDC) modules. Four 32-channel ADC modules and one 128-channel TDC module were used. The data taking window of the ADCs was 2.5 μs. The ADCs discretize the energy signal into 4096 bins. The gain was adjusted so that 1 bin $\approx$ 3 keV.

The trigger thresholds were set as low as possible above the noise, resulting in thresholds ranging from 160 to 240 keV depending on the electronic channel. The trigger efficiency close to threshold was studied with an ^{241}Am source at atmospheric pressure where the range of 5.5-MeV α particles in air is 4 cm [30]. The trigger efficiency was seen to rise rather gently with a typical threshold width[1] of 100 keV. The trigger thresholds quoted above correspond to 50% trigger efficiency. If two or more particles are detected in coincidence, subtrigger signals may be recorded. Low-energy ADC cutoffs ranged from 60 to 230 keV, depending on the channel.

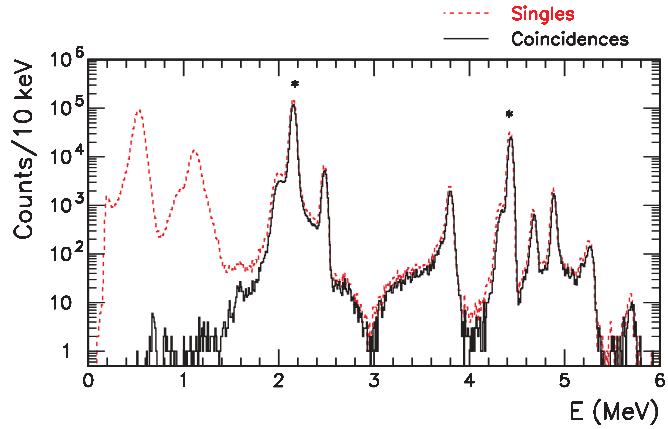

FIG. 4. (Color online) β-delayed α spectrum of ^{20}Na. The dashed curve (red) shows the singles spectrum. The solid curve (black) shows the α spectrum from $\alpha + {}^{16}$O coincidences in opposing DSSSDs. The peaks at 2.15 and 4.43 MeV used for the energy calibration are marked with an asterisk. The corresponding ^{16}O recoil peaks are clearly visible in the singles spectrum at 0.54 and 1.11 MeV.

III. CALIBRATION AND SYSTEMATICS

A. Method of energy calibration

The β-delayed α spectrum of ^{20}Na is shown in Fig. 4. The energy calibration is based on the two most intense α peaks at 2153.3 and 4433.9 keV. Their energies were deduced from the excitation energies, 7421.9(12) and 10 273.2(19) keV, of the corresponding states in ^{20}Ne and the $\alpha + {}^{16}$O threshold energy of 4 729.84(1) keV given in Ref. [31]. Corrections were made for the energy loss of the α particles in the carbon foil and the detector dead layer. In addition, corrections were made for the nonionizing energy loss in the active volume of the detector which does not contribute to the observed signal. A small quadratic correction owing to the nonlinearity of the ADCs, deduced from measurements with a precision pulse generator, was included in the calibration. The correction (measured as the maximum deviation of the quadratic fit with respect to the linear fit) was about 6 keV over the range of measured α energies (0–8.5 MeV).

B. Energy-loss calculation

SRIM 2008 stopping power tables [32] were used to calculate the energy loss experienced by the ions in the carbon foil and the detector dead layer prior to entering the active volume of the detector. The energy loss in the foil

[1]Defined as the length of the energy interval over which the trigger efficiency rises from 10% to 90%.

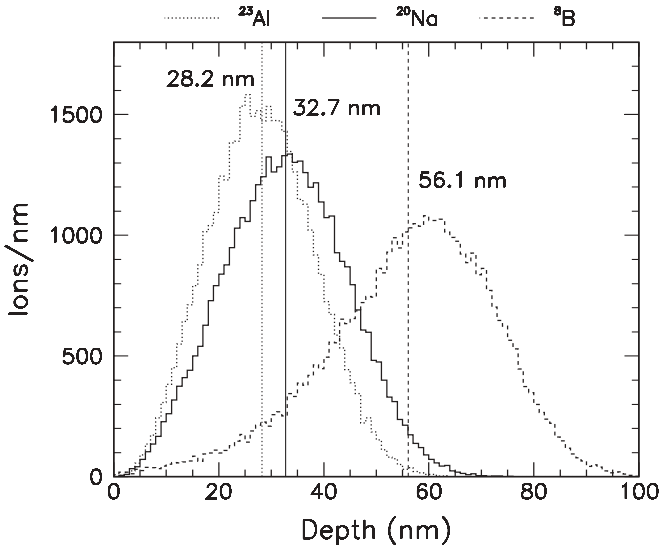

FIG. 5. Implantation depth distributions in carbon at 20 keV obtained from TRIM simulations. Mean values of the distributions are given.

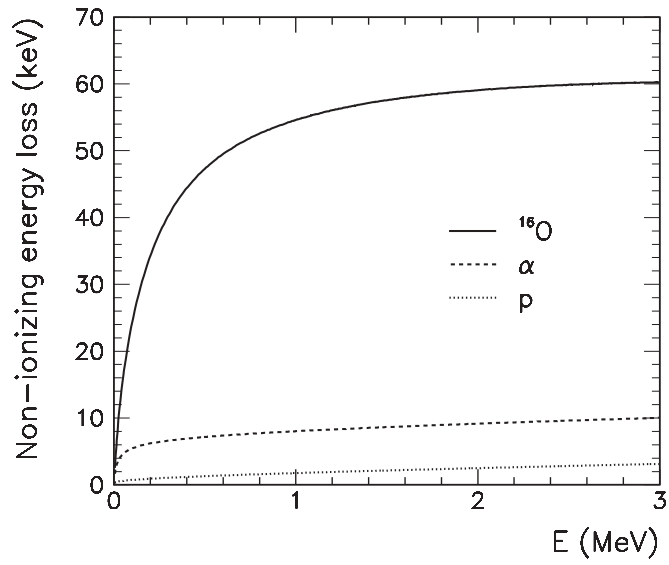

FIG. 6. Nonionizing energy loss of protons, α particles, and ^{16}O ions in Si as a function of the initial ion energy. Obtained from TRIM simulations.

was calculated assuming a fixed implantation depth, thus neglecting the sizable spread shown in Fig. 5. The finite size of the beam spot was also neglected. In both cases, the primary effect will be a broadening of the signal; systematic shifts will only occur at the sub-keV level.

Accurate knowledge of the geometry of the detector setup is necessary to determine the effective foil and dead-layer thicknesses encountered by a particle detected in a particular pixel[2] of the DSSSD. A coarse measurement of the geometry was made prior to insertion of the detectors into the chamber. A more precise determination was achieved using the measured intensity distribution over the surface of the DSSSDs. The accuracy of this method is estimated to be 1 mm based on the comparison of geometries obtained from the different data sets (^{8}B, ^{20}Na, ^{23}Al). Inspection of the distribution of α-α relative angles from the decay of ^{8}B revealed that the DSSSDs were tilted up to a few degrees with respect to the vertical axis.

The nonionizing energy loss in the active volume of the detector was determined from TRIM simulations [32] and is shown in Fig. 6 for the three types of ions detected in the present experiment.

C. Foil and dead-layer thickness

Implantation depth distributions at 20 keV obtained from TRIM simulations are shown in Fig. 5. Experimentally, we may check the TRIM prediction by monitoring the apparent shift in energy of the 2153-keV α peak of ^{20}Na with angle in the two upstream detectors (DSSSDs 1 and 2; see Fig. 3). The α-particle energy must be corrected for the energy loss in the dead layer of the detector, which also exhibits a 3-keV variation with angle. The data are shown in Fig. 7(a).

The implantation depth deduced from the slope of data points is 7.4 ± 0.4 μg/cm^2 or, equivalently, 32.9 ± 1.7 nm, in good agreement with the TRIM prediction.

By monitoring the apparent shift with angle in the two downstream detectors (DSSSDs 3 and 4; see Fig. 3), we may determine the thickness of the foil minus the implantation depth of the ^{20}Na ions. The data are shown in Fig. 7(b). The thickness deduced from the slope is 20.1 ± 0.4 μg/cm^2,

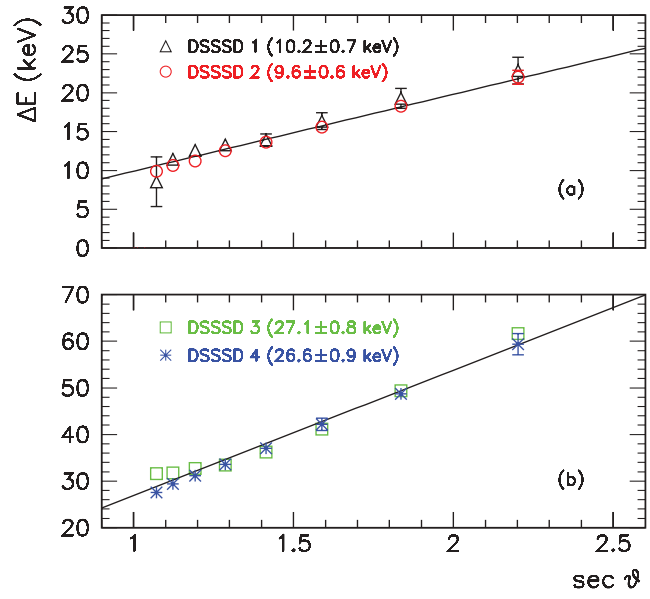

FIG. 7. (Color online) Energy loss of 2153-keV α particles from ^{20}Na in the carbon foil as a function of sec θ, where θ is the angle with respect to the normal to the foil surface. Given in the parentheses are the slopes of the best-fit straight lines, corresponding to the energy loss in the foil at normal exit. Their average is used for the straight lines superimposed on the data points.

[2]Here "pixel" refers to the 3×3 mm^2 geometric overlap of front and back strips. The strips are not physically divided into pixels.

and hence the full thickness of the foil is 27.5 ± 0.6 μg/cm^2. The thickness of the foil was also determined by measuring ^{241}Am with and without the foil placed between the source and the detector. The thickness deduced from this measurement is 23.9 ± 0.5 μg/cm^2. The two values do not agree within the uncertainties, indicating the presence of systematic effects, at the level of 10%, not properly accounted for. One such effect could be gradual changes in thickness across the foil. We take the weighted average, 26 ± 2 μg/cm^2, as our estimate of the foil thickness with the uncertainty increased to account for the large spread.

According to the manufacturer (Micron Technology, Inc.), the DSSSDs have a 100-nm dead layer. The precision of this (mean) value is not stated. Presumably, the precision is around 10%. Because the DSSSDs used in the present experiment were not made from the same Si wafer, we expect variations in dead-layer thickness at the 10% level. Assuming a dead layer of 100 nm in the data analysis, the proton peaks of ^{23}Al have slightly different energies in the four DSSSDs, the difference between the minimum and the maximum energy being 10 keV. By adjusting the dead layers to 85, 75, 120, 105 nm for DSSSDs 1–4, respectively, agreement is obtained. A dedicated measurement of the dead-layer thicknesses was not performed. The 2153-keV α peak of ^{20}Na could not be used to determine the dead-layer thickness because the energy shift with angle was too small. Using the 1110-keV ^{16}O recoil peak it was possible to obtain rough estimates of the dead layers (20% uncertainty) that were in good agreement with the values obtained by the requirement of equal proton energies.

D. Offline measurements with α sources

The α spectrum of ^{241}Am was measured at the beginning of the experiment and at the end. In addition, the α spectra of ^{223}Ra and its α-unstable descendants, ^{219}Rn, ^{215}Po, and ^{211}Bi, were measured at the very end of the experiment. The spectra measured in one selected DSSSD is shown in Fig. 8(a). Deviations from the literature values [33] are shown for all DSSSDs in Fig. 8(b). The deviation observed for ^{211}Bi, away from a linear trend, may be explained as follows: For every successive step in the ^{223}Ra decay chain, the mean depth of the daughter nucleus in the source increases because some recoils escape. Being the last α-emitting isotope in the decay chain, ^{211}Bi will be buried more deeply than any of the other α-emitting isotopes and its α particles subject to the largest energy loss. As discussed in Sec. VI C, it is conceivable that the ^{228}Th calibration of Ref. [19] was distorted by this effect.

For ^{241}Am, the energy loss in the source was measured by varying the orientation of the source relative to the detector while monitoring the shift in peak position. A similar measurement was not performed for the ^{223}Ra source. We find that the energy lost by α particles exiting normal to the source plane is 7 ± 2 keV and have corrected the ^{241}Am energies accordingly. A systematic uncertainty of 2 keV thus applies to the ^{241}Am data points. The energy loss corrections made in connection with the ^{20}Na energy calibration give an additional uncertainty of 3 keV, consistent with the scatter seen for DSSSDs 1–3.

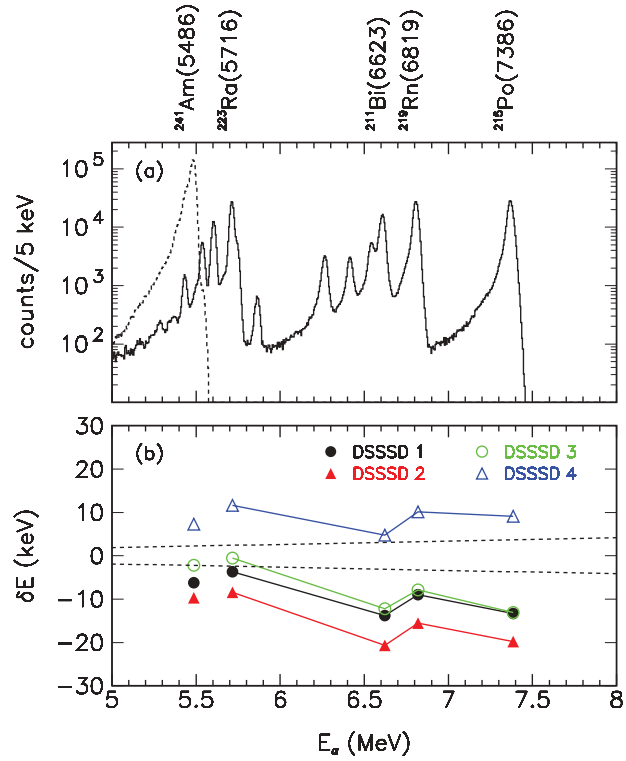

FIG. 8. (Color online) (a) Spectrum from a "cocktail" of α-particle emitters consisting of ^{223}Ra, ^{219}Rn, ^{215}Po, and ^{211}Bi (solid line) and from ^{241}Am (dashed line). (b) Deviations from literature values [33]. The dashed lines mark the $\pm 1\sigma$ uncertainty limits on the energy calibration owing to the uncertainties in the tabulated energies of the β-delayed α peaks of ^{20}Na. Additional uncertainties apply to the data points as discussed in the text.

We conclude that, within the estimated uncertainties, the ^{20}Na online data and the ^{241}Am offline data are consistent from the point of view of DSSSDs 1–3. We are unable to account for the systematic shift of the data in DSSSD 4 relative to the data in DSSSDs 1–3. We note, however, that there is good agreement between all four DSSSDs considering the energies of the 5.26-MeV β-delayed α peak of ^{20}Na and the 8.36-MeV β-delayed α peak of ^{8}B.

E. Nonlinear response at low energy

A careful study of the energy calibration at low energy is important for the determination of the high-energy end of the ^{8}B neutrino spectrum. Below 2 MeV, the following data have been used to test the energy calibration: the β-delayed proton peaks of ^{23}Al with energies between 0.56 and 2.0 MeV; the β-delayed α peaks of ^{20}Na at 0.71, 0.85, and 1.60 MeV; and the two most intense ^{16}O recoil peaks at 0.54 and 1.11 MeV. The deviations are shown in Fig. 9. Note that the energy on the abscissa, E, is the detected energy only, that is, corrected neither for the nonionizing energy loss nor for the energy loss in the carbon foil and the detector dead layer.

The two least energetic β-delayed proton peaks of ^{23}Al observed in the present experiment have also been observed in previous experiments [28,34,35]. The energy of the least

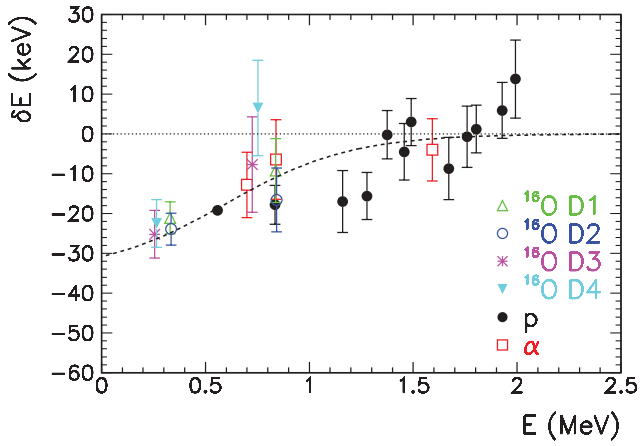

FIG. 9. (Color online) Deviations in the observed energies of a number of low-energy lines, indicating the presence of a quadratic component in the detector response in addition to the quadratic component deduced from the pulse generator measurements. The dashed line is merely meant to guide the eye.

energetic proton peak is particularly well determined through measurements of the ^{22}Na$(p,\gamma)^{23}$Mg reaction [36,37]. The remaining proton peaks have not previously been observed but can, in most cases, be identified with known states in ^{23}Mg. The uncertainties on the tabulated excitation energies of these states [38] dominate the error bars shown in Fig. 9. An overall uncertainty, not shown, of ±4 keV owing to uncertainties associated with the energy-loss corrections, applies to all proton data points. The proton energies have been corrected for the small amount of energy deposited through nonionizing processes (Fig. 6) and the 1.4% pulse height defect given in Ref. [39,40]. A dedicated analysis of the ^{23}Al data will be published separately [41].

The β-delayed α peaks of ^{20}Na at 0.71, 0.85, and 1.60 MeV were observed with limited statistics which accounts for the relatively large error bars. The 1.60-MeV line has been observed previously [42], whereas the 0.71 and 0.85 MeV lines have not. They arise from first-forbidden transitions to two well-known levels in ^{20}Ne. A dedicated analysis of the ^{20}Na data will be published separately [43].

The ^{16}O data in Fig. 9 is shown separately for DSSSDs 1–4. The error bars are dominated by uncertainties associated with the energy-loss correction; larger error bars apply to the most energetic recoils owing to their higher stopping power. The ^{16}O ions lose a substantial amount of energy (about 50 keV) to nonionizing processes (Fig. 6). As noted earlier, we use TRIM simulations to estimate the amount of energy lost to nonionizing processes. It is difficult to estimate the associated uncertainty. We note, however, that the TRIM predictions are about 10 keV below the calculations presented in Ref. [39]. As pointed out in Ref. [44], a recent measurement [45] of the stopping power of ^{7}Li ions in Si gives results that differ substantially from SRIM below 0.1 MeV/nucleon. Based on these observations, we conclude that the uncertainty on the nonionizing energy losses predicted by TRIM is 5–10 keV.

A clear departure from linearity ($\delta E = 0$) is observed in Fig. 9, starting at 1.5 MeV. A plausible explanation for the nonlinear response is that the pulse shape changes at low energies. Because the pulses produced by physical particles have a different time structure compared to the pulses produced by a pulse generator, it is not surprising that the pulse generator measurement failed to uncover this nonlinearity. To test this hypothesis, reliable α-particle data below 1.5 MeV is needed. In this way, uncertainties related to the different response of Si detectors to different kinds of ions will not obscure the interpretation of the data. One way to obtain reliable α-particle data below 1.5 MeV would be to measure the ^{20}Na spectrum with more statistics, which would allow for a more precise determination of the energies of the 0.71- and 0.85-MeV lines. It would, however, also be necessary to reduce the threshold for detecting the associated ^{16}O recoils to reduce certain systematic uncertainties [43]. Another solution would be to measure the β-delayed α spectrum of ^{18}N [46], which produces two narrow α lines at 1.081 and 1.409 MeV, the energy of which is well known [47,48].

F. Single-α detection efficiency

We use the term *single-α detection efficiency* to mean the probability that an α particle is detected if it strikes one of the DSSSDs. Owing to the arrangement of the detectors and the fact that the α particles from the decay of ^{8}B are being emitted approximately back to back, the detection of an α particle in the central 6×6 pixels of one detector, guarantees that a second α particle must have struck the opposite detector (cf. Sec. IV). Therefore, the single-α detection efficiency of the opposite detector can be determined by keeping count of how often the second α particle is detected, that is, by evaluating the coincidences-to-singles ratio. Figures 10(a) and 10(b) show the coincidences-to-singles ratio in DSSSD 4, corresponding to the single-α detection efficiency of DSSSD 1.

The single-α detection efficiency exhibits a weak energy dependence, dropping from 97.0% at 1 MeV to 96.3% at 8 MeV. As demonstrated in Fig. 10(c), the rapid drop in the coincidences-to-singles ratio below 0.7 MeV is caused by the presence of a low-energy background component in the singles spectrum, the intensity of which is consistent with the expected β background.[3] Owing to this low-energy background component, we are unable to determine the single-α detection efficiency of the DSSSDs below ≈0.7 MeV. We assume that the efficiency remains fairly constant, as shown by the solid (red) curve in Fig. 10(a) which represents our estimate of the single-α detection efficiency over the entire energy range. The single-α detection efficiencies of DSSSDs 2–4 are very similar to that of DSSSD 1. The extent of the background component in the singles spectrum does, however, vary somewhat. In DSSSD 1, for instance, the coincidences-to-singles ratio already begins to drop around 1.0 MeV.

[3]The energy loss of minimum-ionizing β particles in Si is 0.4 keV/μm. Given that the DSSSDs are 60 μm thick, the typical energy deposited by β particles is only 24 keV. β particles subject to significant straggling may, however, deposit considerably more energy.

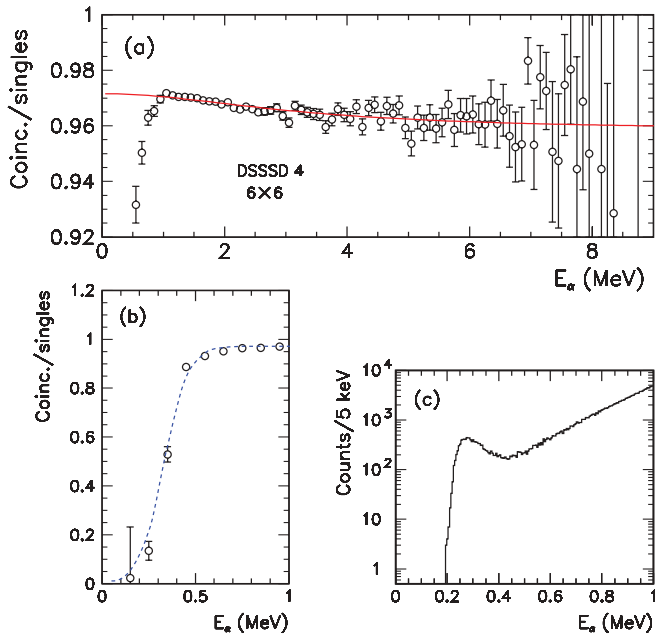

FIG. 10. (Color online) (a),(b) Coincidences-to-singles ratio in the central 6×6 pixels of DSSSD 4. The solid (red) curve is our estimate of the single-α detection efficiency of DSSSD 1. The dashed (blue) curve is merely meant to guide the eye. (c) α spectrum measured in DSSSD 4. The low-energy background component is seen to dominate the spectrum below 0.4 MeV and contributes up to 0.7 MeV.

The main reason for the observed reduction in the single-α detection efficiency is charge sharing between neighboring strips [49] which may occur when an α particle strikes the 100-μm interstrip spacing. Such events are normally discarded in the analysis, but they can, to a large extent, be recovered if desired. An analysis of recovered sharing events has been performed and shows that charge sharing indeed occurs with a probability of 3%. The sharing probability is relatively constant above 2 MeV, but drops below 2 MeV, consistent with the observed increase in the single-α detection efficiency. The sharing probability is also found to be weakly dependent on the angle of incidence, the probability being largest for normal incidence.

G. Response function

We use the term *response function* to mean the distribution of energies measured from a perfectly monochromatic source owing to experimental effects. Below, we discuss how the response function is best extracted from the experimental data.

The β decay of the 2^+, $T = 1$ ground state of ^{20}Na to the isobaric analog state (IAS) in ^{20}Ne at 10 273.2 keV excitation energy, produces the second-most-intense peak in the β-delayed α spectrum at 4434 keV (see Fig. 4). The IAS in ^{20}Ne and the ground state of ^{20}Na have the same quantum numbers and similar structures. The width of the IAS is $\leqslant$0.3 keV [31]. The energies of the α particles emitted in its decay are smeared out owing to the recoil motion of ^{20}Ne. For a pure Fermi transition, the broadening effect can be approximated as [50]

$$\rho(x) = \begin{cases} \frac{5}{8\delta E_{\max}}(1 - x^4) , & -1 \leqslant x \leqslant 1, \\ 0 , & |x| > 1, \end{cases} \tag{1}$$

with $x = \delta E/\delta E_{\max}$, where $\delta E = E_\alpha - \langle E_\alpha \rangle$ is the shift relative to the mean α-particle energy, and the maximum shift is given by

$$\delta E_{\max} = \frac{m_e}{M}\left[2Qm_\alpha c^2\left(W_0^2 - 1\right)\frac{Mc^2 - m_\alpha c^2 - Q}{Mc^2 - Q}\right]^{1/2}, \tag{2}$$

where m_e, m_α, and M are the electron, α-particle, and ^{20}Ne masses, $Q = E_x - Q_\alpha$ where E_x is the excitation energy in ^{20}Ne and $Q_\alpha = 4729.84(1)$ keV is the $\alpha + {}^{16}$O threshold energy, and $W_0 = (E_0 - E_x)/m_e c^2$ where $E_0 = 13\,375(7)$ keV is the maximum total β energy for decays to the ground state of ^{20}Na. For the IAS in ^{20}Ne, one obtains $\delta E_{\max} = 29.9$ keV. The transition to the IAS is known [42] to be a mixed Fermi and Gamow-Teller type transition. The Gamow-Teller component is, however, rather small, so the broadening effect is well described by Eq. (1). Only little interference between the IAS and neighboring 2^+ states, which could potentially distort the shape of the 4434-keV peak, is expected owing to the unique structure and $T = 1$ nature of the IAS. We conclude that the *physical* shape of the 4434-keV peak is well understood, and hence this provides an excellent case for studying the modifications of the shape caused by *experimental* effects.

We adopt the parametrization of Ref. [20] to describe the response function owing to experimental effects. It consists of a Gaussian folded through two low-energy exponential tails,

$$\psi(E_0, E) = \sum_{i=1}^{2} \frac{A_i}{2\lambda_i} \exp\left(\frac{E - E_0}{\lambda_i} + \frac{\sigma^2}{2\lambda_i^2}\right) \times \operatorname{erfc}\left(\frac{E - E_0 + \sigma^2/\lambda_i}{\sqrt{2}\sigma}\right), \tag{3}$$

where E_0 and E are the nominal and observed energies, λ_i are the exponential decay lengths, and erfc is the complement of the incomplete error function. The normalization coefficients are $A_1 = 1/(1 + r)$ and $A_2 = r/(1 + r)$, with r being the relative area of tail 2 compared with tail 1. Because Eq. (3) merely serves as a useful parametrization, we shall not be concerned with the physical origin of the exponential tails.

Ions striking the aluminum grid that covers 4% of the detector surface experience an additional energy loss compared to other ions and therefore give rise to a low-energy satellite peak. We expect the satellite to be wider than the main peak owing to the larger variation in effective thickness with angle. Therefore, the complete response function reads

$$\Psi(E_0, E) = (1 - g)\,\psi(\sigma; E_0, E) + g\,\psi(\sigma_g; E_0 - E_g, E), \tag{4}$$

where E_g is the mean energy loss in the grid, σ is the Gaussian width of the main peak, σ_g is the Gaussian width of the satellite peak, and g is the fraction of the detector surface covered by the aluminum grid.

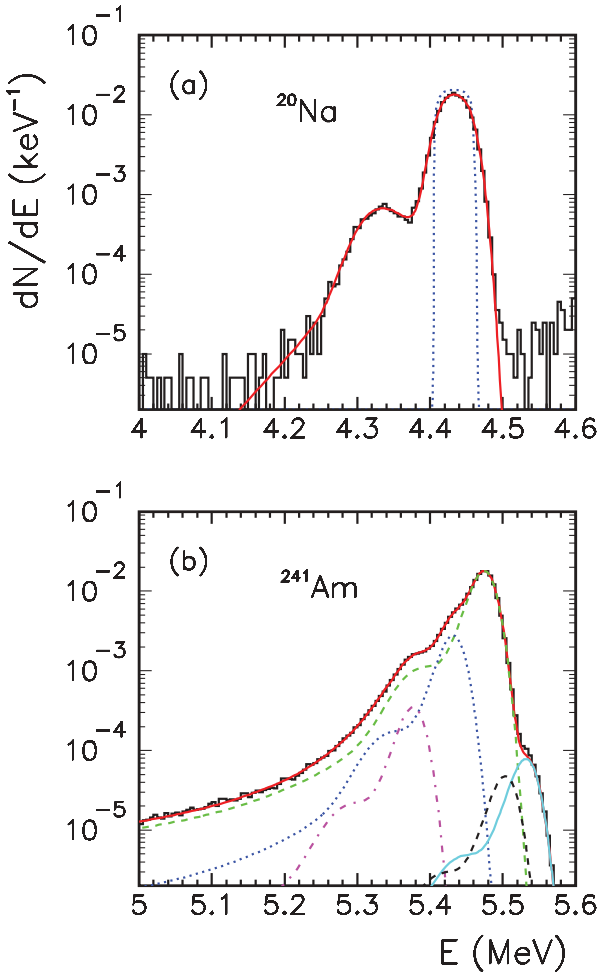

FIG. 11. (Color online) (a) β-delayed α spectrum of ^{20}Na between 4 and 4.6 MeV measured in DSSSD 1. The dotted blue curve shows the recoil broadening distribution computed from Eq. (1). The solid red curve shows the best fit to the data using Eq. (5). (b) α spectrum of ^{241}Am between 5 and 5.6 MeV measured in DSSSD 1. The solid red curve shows the best fit to the data. The decomposition into the individual α peaks is also shown. Both spectra have been normalized to unit area.

The line shape of the 4434-keV peak, including experimental effects, is given by the convolution of the response function [Eq. (4)], with the recoil broadening distribution [Eq. (1)], that is,

$$\frac{dN}{dE} = \int \Psi(E_\alpha, E)\, \rho[x(E_\alpha)]\, dE_\alpha. \qquad (5)$$

Figure 11(a) shows the line shape measured in DSSSD 1 with the recoil broadening distribution and the best fit using Eq. (5) superimposed. The α-particle energy has been corrected for the energy loss in the foil and the detector dead layer, taking into account the variation in effective thickness with angle but assuming a fixed implantation depth in the foil.

This procedure gives a reliable determination of the response function, $\Psi(E_0, E)$, at 4434 keV. To determine the response function for a general α-particle energy, we make the assumption that the exponential tails are independent of energy. We convert the energy loss in the aluminum grid, E_g, into an equivalent thickness (0.60 μm), which we use to calculate the energy loss in the grid for other α-particle energies. Finally, we assume the Gaussian width of the satellite peak, σ_g, to be proportional to E_g. While the combined intensity of the satellite peak and the exponential tails is well determined by the fit, the relative intensity of the two components is not strongly constrained. Because the satellite peak depends on the energy whereas the exponential tails are assumed independent of energy, this introduces some uncertainty in the extrapolation procedure outlined above. However, the good agreement between the experimental and simulated recoil broadening distributions for the decay of ^{8}B (cf. Sec. IV D) give us confidence in the extrapolation procedure and constrains the contribution of the satellite to $4.0 \pm 0.5\%$ in agreement with expectations.

For the analysis of the ^{8}B data, the quantity of interest is the ^{8}Be excitation energy, E_x, computed as the sum of the α-particle energies. We calculate the sum-energy response function as

$$\Psi_{n_1+n_2}(E_x) = \int \Psi_{n_1}(E_1)\, \Psi_{n_2}(E_x - E_1)\, dE_1, \qquad (6)$$

where $\Psi_{n_1}(E_1)$ and $\Psi_{n_2}(E_2)$ are the single-α response functions of detectors n_1 and n_2.

Figure 11(b) shows the α spectrum of ^{241}Am measured in DSSSD 1. Five individual α peaks of known energies and intensities [33] contribute to the distribution. The response function defined by Eq. (4) has been used for the fit. The thickness and area of the aluminum grid deduced from the fit agrees with the corresponding values deduced from the fit to the 4434-keV peak. However, there are also differences: the Gaussian width is roughly 30% larger and, as is readily visible, the exponential tails are more pronounced. These differences are likely to be a consequence of energy loss processes taking place in the ^{241}Am source. As discussed in Sec. VI C, this could have affected the energy determination of Ref. [20]. We stress that the present analysis uses the response function deduced from the ^{20}Na data.

H. Temporal variations

At the end of the ^{8}B run, the foil thickness was determined following the procedure described in Sec. III C, and it was found that the thickness had increased by 20% during the run. As expected, the implantation depth was found to be unchanged. There seems to be two possible explanations for the increase in foil thickness: either an additional, very intense, beam component or contaminating gas, for example, hydrocarbons from pump oil. The average beam intensity required to explain the observed increase can be estimated to be 10^{11} pps. A beam component of this intensity *and* with the appropriate mass-to-charge ratio to pass through the separator seems unlikely. We conclude that a contaminant gas originating from the pumping system constitutes the most plausible explanation for the observed increase in foil thickness.

The signal from a precision pulse generator was fed to the preamplifiers throughout the entire experiment to monitor the

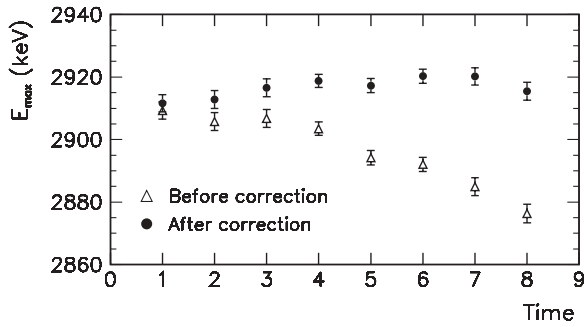

FIG. 12. Maximum of the E_x distribution (not corrected for the recoil energy, E_R) as a function of time before and after the correction for the drift in electronic gain and increase in foil thickness.

stability of the energy calibration. The signal was placed at 9 MeV, well above the end point of the α-particle spectrum. A slow drift of 5–15 keV, depending on the electronic channel, was observed, in both front and back strips. Toward the end of the ^{8}B run, the resolution in the front strips of DSSSDs 1 and 2 deteriorated considerably from 30 keV to around 60 keV (full width at half maximum). In contrast, the resolution of the back strips was unchanged. In DSSSD 4, both front- and back-strip resolution was unchanged, whereas in DSSSD 3 the resolution worsened over the course of the experiment in both front and back strips, but only by 20%–30%. Given the deteriorating resolution in the front strips of DSSSDs 1 and 2, we have used the back strips for energy determination. For consistency, we do this in all four DSSSDs. The front-strip energies have only been used for the matching of front and back signals (a time-dependent tolerance was adopted to account for the deteriorating resolution in the front strips).

By comparing the ^{20}Na and ^{23}Al data taken before and after the ^{8}B run, it was possible to estimate the shift in electronic gain at low energies. At the peak of the ^{8}B singles-α spectrum (1.5 MeV), the shift was 5–10 keV, depending on the electronic channel, that is, slightly smaller than the shift observed at 9 MeV with the pulse generator signal.

The drift in electronic gain and the increase in foil thickness have been taken into account by assuming that the changes occur linearly in time. The effect of this correction is seen in Fig. 12, which shows the evolution in the maximum of the E_x distribution during the measurement. The 72-h-long measurement has been divided into eight bins of approximately 9 h duration each.

IV. THEORY AND SIMULATION

Below we discuss the kinematics and the correlations in the β decay of ^{8}B, allowing us to determine the recoil correction, E_R , and to determine the α-α coincidence detection efficiency of the setup.

A. Kinematics

A schematic illustration of the kinematics of the β decay of ^{8}B is given in Fig. 13. In the rest frame of the daughter nucleus, ^{8}Be, referred to as the recoil frame, the two α particles

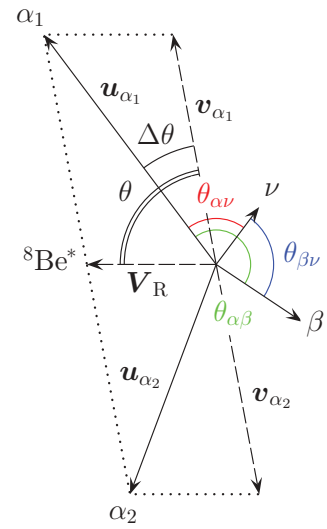

FIG. 13. (Color online) Kinematics of the β decay of ^{8}B.

travel at equal speeds in opposite directions, that is, $\boldsymbol{v}_{\alpha_2} = -\boldsymbol{v}_{\alpha_1}$. The velocities of the α particles in the rest frame of ^{8}B, referred to as the laboratory frame, are obtained by simple vector addition, $\boldsymbol{u}_{\alpha_i} = \boldsymbol{v}_{\alpha_i} + \boldsymbol{V}_R$, where $\boldsymbol{V}_R$ is the ^{8}Be recoil velocity. Squaring and multiplying by $\frac{1}{2}m_\alpha$, we obtain the α-particle kinetic energies in the laboratory frame,

$$\begin{aligned} E_{\alpha_i} &= \frac{1}{2}m_\alpha u_{\alpha_i}^2 \\ &= \frac{1}{2}m_\alpha v_{\alpha_i}^2 + \frac{1}{2}m_\alpha V_R^2 + m_\alpha \boldsymbol{v}_{\alpha_i}\cdot\boldsymbol{V}_R \\ &= E_\alpha^* + \frac{m_\alpha}{M}E_R \pm 2\sqrt{\frac{m_\alpha}{M}E_\alpha^* E_R}\cos\theta, \end{aligned} \tag{7}$$

where $E_R = \frac{1}{2}MV_R^2$ is the ^{8}Be recoil energy, M is the ^{8}Be mass, and $E_\alpha^* = \frac{1}{2}(E_x + 92\ \text{keV})$ is the α-particle kinetic energy in the recoil frame, E_x being, as always, the excitation energy in ^{8}Be. With the angle θ chosen as shown in Fig. 13, the plus sign applies to α_1 and the minus sign to α_2. Adding the two α-particle laboratory energies, we obtain

$$E_{\alpha_1} + E_{\alpha_2} = 2E_\alpha^* + E_R = E_x + 92\ \text{keV} + E_R, \tag{8}$$

owing to the cancellation of the last term in Eq. (7). Apart from the small correction given by the recoil energy, E_R, the total energy of the α particles equals the excitation energy in ^{8}Be plus the 92-keV gap separating the ground state of ^{8}Be and the $\alpha + \alpha$ threshold. The recoil energy attains its maximum value when the leptons are emitted in the same direction. Momentum conservation gives $E_{R,max} \approx (E_0 - E_x)^2/2Mc^2$, where $E_0 = Q_\beta + m_e c^2 = 17.4688(10)$ MeV is the maximum total β energy for decays to the ground state of ^{8}Be. For $E_x = 3$ MeV, one obtains $E_{R,max} = 14$ keV. When averaged over the lepton angles, the recoil energy is reduced to 7.3 keV. The E_x dependence of the average recoil energy, determined by the simulation discussed below, is shown in Fig. 14.

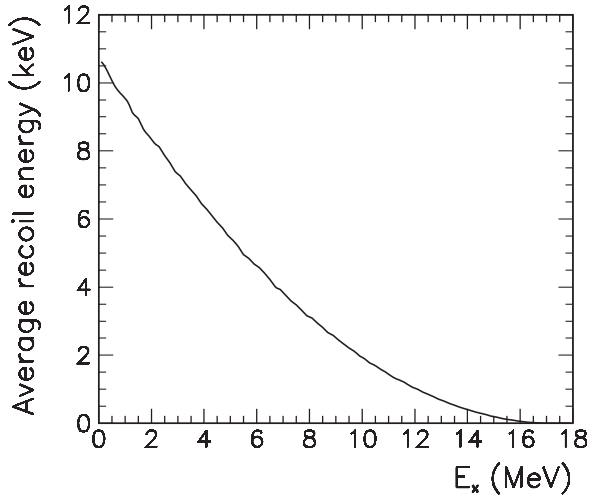

FIG. 14. Average recoil energy as function of the ^{8}Be excitation energy, E_x.

B. β-ν-α correlation

Neglecting the so-called *recoil terms* of order E_β/Mc^2 where E_β is the total β energy, the β-ν-α triple correlation function, $W(p_\beta, \theta_{\beta\nu}, \theta_{\alpha\beta}, \theta_{\alpha\nu})$, is given by Eq. (5) in Ref. [42]. Note that W depends on E_x through the maximum total β energy which is called $E_0 - E_x$ in the present notation but is called E_0 in Ref. [42]. For ^{8}B we have $E_\beta/Mc^2 < 2 \times 10^{-3}$, so recoil terms may safely be neglected. Often it is also possible to neglect the so-called *kinematic terms* of order $E_\beta/Mv_\alpha c$ where v_α is the speed of the α particle in the recoil frame. However, in the present case, the ratio $E_\beta/Mv_\alpha c$ can attain quite large values, for example, up to 0.13 for $E_x = 1$ MeV. Therefore, we retain the kinematic terms. In calculating W, we assume a pure Gamow-Teller decay, implying a triple-correlation coefficient of $a_3 = -1$. For the present spin sequence, $2^+ \to 2^+ \to 0^+$, the spin-dependent coefficients called ξ and $heta$ in Ref. [42], take on the values 10 and 1, respectively.

C. Monte Carlo simulation

We adopt the following procedure to simulate the β decay of ^{8}B for a fixed excitation energy, E_x: The directions of the neutrino (ν) and the positron (β) in the laboratory frame are chosen randomly relative to the direction of α_1 in the recoil frame. The kinetic energy of the positron, T_β, is chosen randomly from 0 to the maximum possible value, $T_{\beta,\max} = Q_\beta - E_x$, where $Q_\beta = E_0 - m_e c^2$. The neutrino energy is calculated as $E_\nu = T_{\beta,\max} - T_\beta$. The ^{8}Be recoil momentum is determined by the requirement of momentum conservation, $\boldsymbol{p}_\mathrm{R} = -(\boldsymbol{p}_\beta + \boldsymbol{p}_\nu)$. The recoil energy is calculated as $E_\mathrm{R} = p_\mathrm{R}^2/2M$. The laboratory velocities of the α particles, $\boldsymbol{u}_{\alpha_i}$, are obtained from the recoil-frame velocities, $\boldsymbol{v}_{\alpha_i}$, by simple vector addition, $\boldsymbol{u}_{\alpha_i} = \boldsymbol{v}_{\alpha_i} + \boldsymbol{V}_\mathrm{R}$ with $\boldsymbol{V}_\mathrm{R} = \boldsymbol{p}_\mathrm{R}/M$. The phase-space factor is calculated as $f = (Q_\beta - E_x - T_\beta)^2 p_\beta (T_\beta + m_e c^2)$. [For the R-matrix analysis (cf. Sec. VI) a more elaborate expression [51] is used.] The triple correlation amplitude, W, is calculated as discussed above. Finally, the amplitude of the event is calculated as $A = fW$.

To simulate a distribution of excitation energies, $\mathcal{F}(E_x)$, we generate random values of E_x within the limits set by energy conservation and calculate the amplitude as $A = fW\mathcal{F}$. Note that the phase-space factor, f, must be properly normalized.

Using the Von Neumann sampling technique, we generate a *realistic* sample of decay events which we subject to the experimental conditions: We check whether the α particles hit the detectors. We calculate the energy loss in the carbon foil and the detector dead layers assuming a uniform spherical beam spot of 7 mm diameter and using the TRIM implantation depth distribution (Fig. 5). We take into account the detector response function (Sec. III G) which exhibits exponential tails as well as a low-energy satellite peak. We check that the α-particle energies are above detection threshold. Finally, we take into account the single-α detection efficiency discussed in Sec. III F. To account for any bias introduced by the various cuts and gates imposed on the experimental data, we pass the simulated data through the same analysis program as used for the experimental data.

D. α-α recoil broadening

The third term in Eq. (7) averages to zero but causes a substantial broadening of the α-particle energy spectrum; that is, for fixed E_x we measure a *distribution* of α-particle energies in the laboratory, the width of which depends on E_x. Figure 15 shows the energies of α-α coincidences detected in DSSSD 1 and 4. By placing cuts on E_x and evaluating the shift relative to the mean α energy as $\delta E = \frac{1}{2}(E_{\alpha_1} - E_{\alpha_2})$, we obtain the distributions shown in Fig. 16. The distribution of excitation energies, $\mathcal{F}(E_x)$, used in the simulation is the one determined from the present study. The experimental and simulated δE distributions are in good agreement in all three cases, giving general confidence in the simulation. Note that the simulation

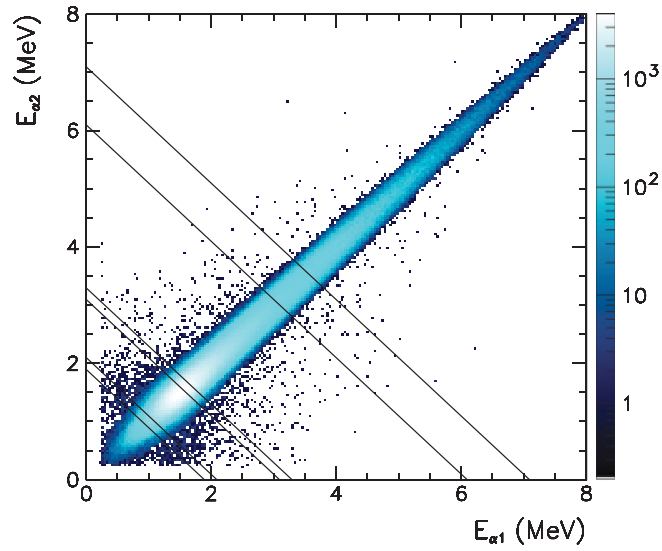

FIG. 15. (Color online) Two-dimensional energy spectrum of α-α coincidences detected in DSSSDs 1 and 4 (using only the central 6×6 pixels of DSSSD 1). The transversal bands show the excitation energy cuts used to generate Figs. 16(a)–16(c).

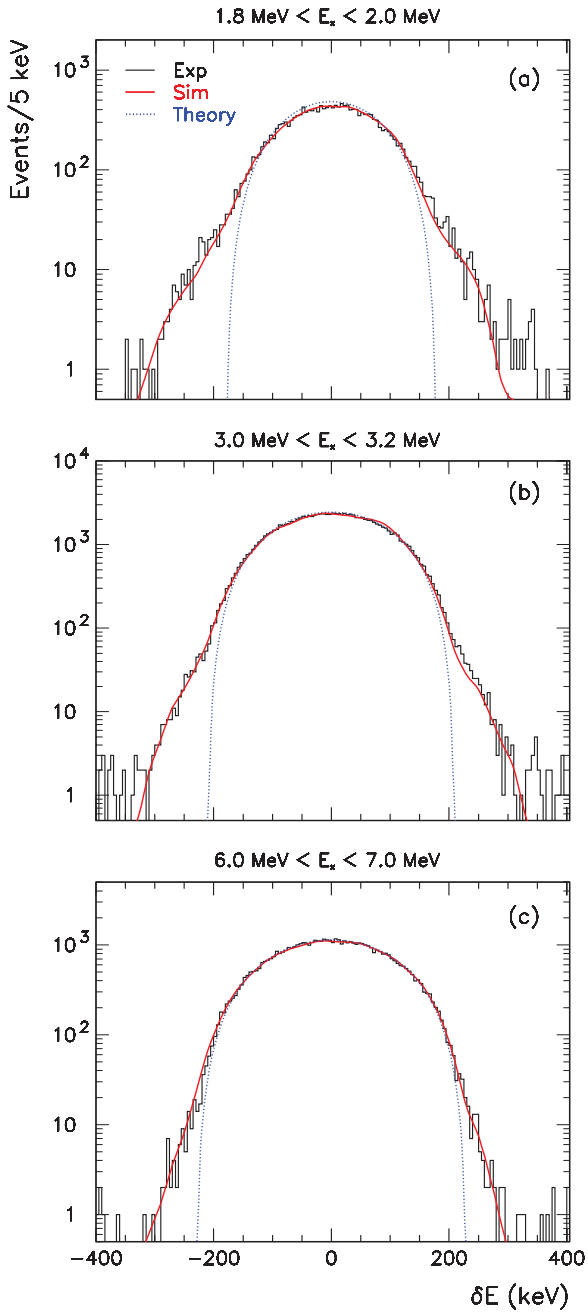

FIG. 16. (Color online) α-α recoil-broadening distributions for three different cuts on the excitation energy. δE is the shift relative to the mean α energy, that ism $\delta E = \frac{1}{2}(E_{\alpha_1} - E_{\alpha_2})$. The histogram (black) is the experimental data. The solid (red) and dotted (blue) curves, labeled "Sim" and "Theory," are the result of the simulation with and without experimental effects, respectively.

is able to reproduce the response tails, indicating that the experimental effects are well understood.

E. Coincidence detection efficiency

As illustrated in Fig. 13, the recoil motion of the ^{8}Be nucleus implies an angular shift, $\Delta\theta$, for the α particles in the laboratory frame. The combination of a large Q value and a light daughter nucleus makes this an important effect for the ^{8}B decay. The smaller the E_x, the larger is the maximum angular shift, $\Delta\theta_{\max}$. One may easily show that $\Delta\theta_{\max} = 3.9^\circ$ for $E_x = 3$ MeV, corresponding to an α-α opening angle of $180^\circ - 2 \times 3.9^\circ = 172^\circ$.

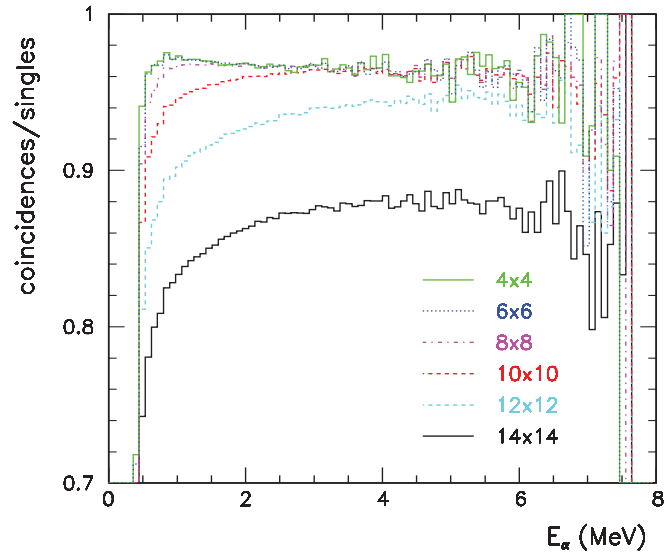

FIG. 17. (Color online) Coincidence-to-singles ratio in DSSSD 4. The curve labeled 14×14 is obtained by requiring that the α particle striking DSSSD 4 is within the central 14×14 pixels, the curve labeled 12×12 by requiring that it is within the central 12×12 pixels, etc.

Owing to this energy-dependent angular shift, the probability for detecting α-α coincidences in oppositely facing detectors drops at small excitation energies. This is clearly seen in Fig. 17, which displays the coincidence-to-singles ratio in DSSSD 4 as a function of the α-particle energy measured in DSSSD 4. The curve labeled 14×14 is obtained by requiring that the α particle striking DSSSD 4 is within the central 14×14 pixels, the curve labeled 12×12 by requiring that it is within the central 12×12 pixels, etc. The more central we require the hit in DSSSD 4 to be, the more likely it is for the partner α particle to hit DSSSD 1, and the drop in the coincidence-to-singles ratio is correspondingly less marked. For the two most central cuts, 6×6 and 4×4, the drop is essentially absent. The sharp drop around 0.7 MeV that occurs in all spectra is attributable to the presence of a low-energy background component in the singles spectrum (Sec. III F). Though unaffected by the angular shift, the 4×4 and 6×6 coincidence-to-singles ratios still exhibits a weak energy dependence. This is understood as resulting from an energy dependence in the single-particle detection efficiency (Sec. III F).

Using the simulation program, we obtain the coincidence detection efficiency curves shown in Fig. 18. The physical effects responsible for the features of the curves are indicated. Using these curves, we correct the experimental coincidence spectra. Figure 19 shows the ratio of the 14×14 and the 6×6 coincidence spectrum before and after the correction. The agreement between the 14×14 and the 6×6 coincidence spectrum is seen to improve considerably (ratio

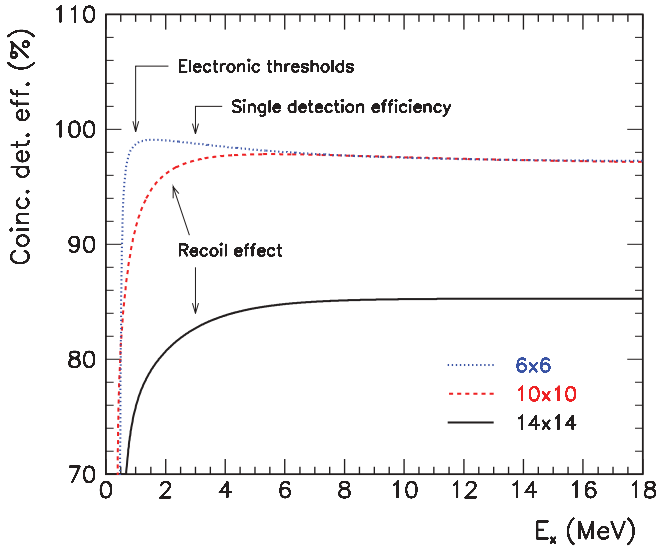

FIG. 18. (Color online) Simulated coincidence detection efficiency in DSSSD 1 + 4 considering three different subsets of DSSSD 4.

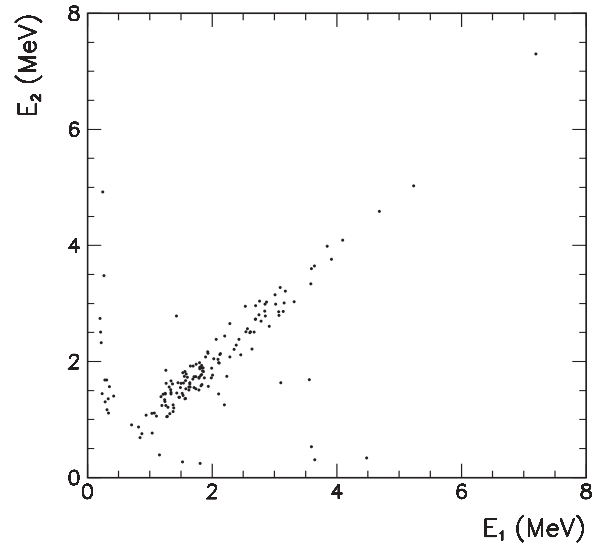

FIG. 20. Two-dimensional energy spectrum of α-α coincidences detected in DSSSDs 1 and 3, which are adjacent to one another. Only the central 6 × 6 pixels of DSSSD 1 are considered.

nearly constant) when the efficiency correction is applied. The nearly constant ratio of ≈4.6 corresponds to the ratio of the solid angles subtended by the 14 × 14 and 6 × 6 selections. The large fluctuations arise because we compare overlapping data sets.

To minimize systematic uncertainties, we discard the 14 × 14 coincidence spectrum despite the apparent success of the efficiency correction. In the following analysis, we use the 6 × 6 coincidence spectrum up to $E_x = 10$ MeV. Above $E_x = 10$ MeV, we use the 10 × 10 coincidence spectrum to gain more statistics. As Fig. 18 clearly demonstrates, the 10 × 10 coincidence spectrum is only subject to geometry-dependent corrections below $E_x \sim 7$ MeV.

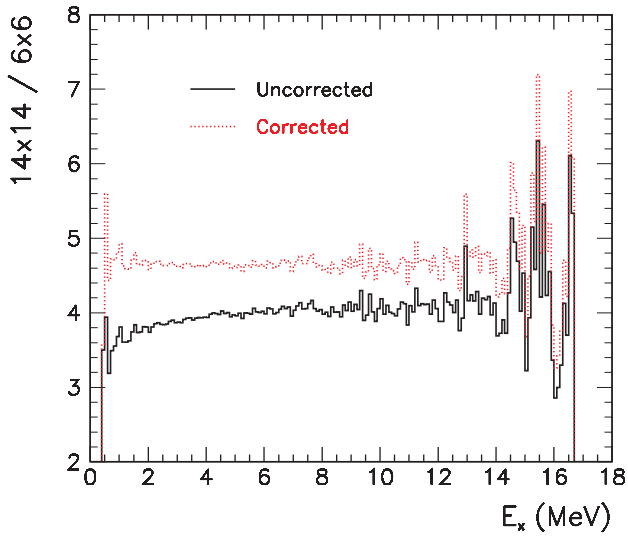

FIG. 19. (Color online) Ratio of the 14 × 14 and the 6 × 6 coincidence spectrum with and without the coincidence detection efficiency correction.

V. DATA ANALYSIS

Below, we examine the various types of multiparticle events found in the data, we discuss the best way of determining E_x from the measurement of the α-particle momenta, and we estimate the uncertainty in the determination of E_x.

A. Multiparticle events

In addition to the numerous α-α events, the following types of multiparticle events are found in the data.

α-α-β coincidences. Because the energy deposited by the positrons in the DSSSDs (on average 0.4 keV/μm × 60 μm = 24 keV for minimum ionizing positrons) typically is far below detection threshold, α-α-β coincidences are rare: 1.0×10^4 events of this type were detected compared to 1.1×10^7 α-α coincidences. The identification of the positron is usually straightforward but becomes problematic for α energies below ∼0.5 MeV.

α-β coincidences. Owing to the large α-α coincidence detection efficiency of the setup, α-β coincidences are even rarer than α-α-β coincidences. The presence of α-β coincidences in the data is most easily demonstrated by considering coincidences in adjacent rather than opposite detectors, as shown in Fig. 20. The events close to the axes represent α-β coincidences while the events on the diagonal represent α-α coincidences with unphysically large α-α opening angles, possibly owing to one α particle being scattered by the frame supporting the carbon foil.

Random coincidences. Given the ADC detection window of 2.5 μs, the ^{8}B implantation rate of 2.0×10^2 ions per second, and the 30% solid-angle coverage, random coincidences between successive ^{8}B decay events occur with a probability of 2×10^{-4}. Owing to the large α-α coincidence detection efficiency of the setup, most random coincidences have multiplicity three or four and hence are easily identified.

Because the events are uncorrelated, they may be disregarded from the analysis without influencing the spectrum.

B. Determination of E_x

We note that β summing can safely be neglected thanks to the high granularity and thinness of the DSSSDs. The shift in E_x caused by β summing may be estimated to be 0.3 keV.

Given the knowledge of both α-particle laboratory momenta, E_x can be determined in two ways: either using Eq. (8) or using the relation

$$\frac{(\boldsymbol{p}_{\alpha_1} - \boldsymbol{p}_{\alpha_2})^2}{4m_\alpha} = E_x + 92\ \text{keV}, \tag{9}$$

which is easily verified. The advantage of using Eq. (9) is that knowledge of the recoil energy, E_R, is unnecessary. The disadvantage is that additional uncertainties are introduced, as Eq. (9) relies on knowledge not only of the energies but also of the directions of the α particles and thus on the geometry of the setup. We find that the spectra obtained using Eqs. (8) and (9) are shifted relative to one another by 3 keV, which corresponds to an error of 2–3 mm in the assumed geometry, in reasonable agreement with the estimated uncertainty of 1 mm (Sec. III B). In the following analysis, we rely on Eq. (8) which we consider to provide the most reliable determination of E_x.

Using the following subsets of the experimental data, we determine four different E_x distributions:

(I) coincidences in DSSSDs 1 and 4 with an α particle striking the central 6×6 (10×10 above $E_x = 10$ MeV) pixels in DSSSD 1;
(II) coincidences in DSSSDs 1 and 4 with an α particle striking the central 6×6 (10×10 above $E_x = 10$ MeV) pixels in DSSSD 4;
(III) coincidences in DSSSDs 2 and 3 with an α particle striking the central 6×6 (10×10 above $E_x = 10$ MeV) pixels in DSSSD 2;
(IV) coincidences in DSSSDs 2 and 3 with an α particle striking the central 6×6 (10×10 above $E_x = 10$ MeV) pixels in DSSSD 3.

The presence of a dead strip in DSSSD 3 implies a larger uncertainty on the efficiency correction of spectrum III, and hence this spectrum is discarded. Spectra I and II are preferred over IV owing to some atypical and not fully understood features of the response of DSSSD 3. Because the data content of I and II overlap, only one may be selected for further analysis. We randomly chose II and use I and IV for checks of consistency. Impressively, the maxima of I, II, and IV agree within ± 2 keV.

C. Uncertainty in the determination of E_x

The determination of E_x is associated with a number of uncertainties.

(i) *Temporal.* Based on Fig. 12, the contribution to the overall E_x uncertainty from the drift in electronic gain and the increase in foil thickness is estimated to be 3 keV.
(ii) *Response.* Owing to the asymmetric shape of the response function (Sec. III G), the maximum of the observed E_x distribution is shifted 19 keV down in energy compared to the maximum of the actual (physical) E_x distribution. By varying the parameters describing the response function within their estimated uncertainties, the uncertainty on the shift is determined to be 2 keV.
(iii) *Quadratic.* We assume a 20% uncertainty on the low-energy quadratic component (Sec. III E).
(iv) *Calibration.* The uncertainties on the tabulated level energies in ^{20}Ne translate into uncertainties on the energies of the two β-delayed α peaks of ^{20}Na used for the calibration.
(V) *Energy loss.* A 10% uncertainty is assumed for the foil thickness and the detector dead layers. We note that E_x is insensitive to errors in the assumed implantation depth because the errors cancel when the two α energies are added up.

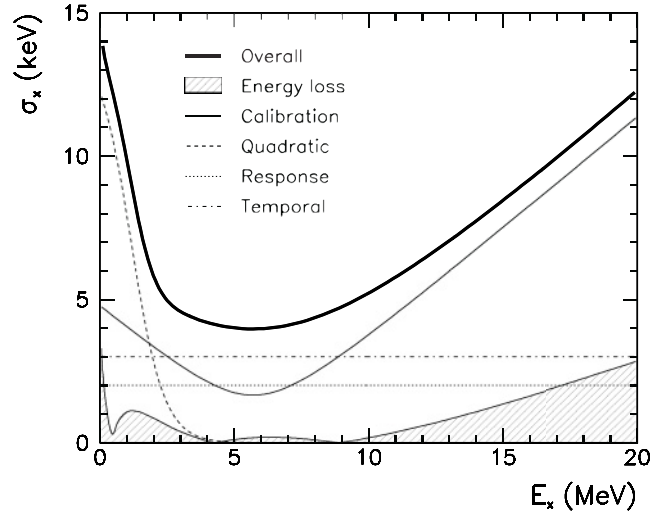

FIG. 21. Estimated magnitudes of the uncertainties affecting the determination of E_x.

Our estimates of the magnitude, σ_x, of the uncertainties affecting the determination of E_x are shown in Fig. 21. The thick solid curve represents our estimate of the overall uncertainty. Below 2 MeV, the uncertainty associated with the low-energy quadratic component dominates. Above 9 MeV, the uncertainties on the energies of the two β-delayed α peaks of ^{20}Na used for the calibration dominate. In the peak region, the overall uncertainty is estimated to be 5 keV.

VI. RESULTS AND DISCUSSION

A. *R*-matrix parameterization

A parametrization of the E_x distribution, $\mathcal{F}(E_x) = dN/dE_x$, is not essential for the purpose of calculating the ^{8}B neutrino spectrum but does offer some advantages. It facilitates the propagation of systematic uncertainties and simplifies

the treatment of the experimental response. Furthermore, a physically meaningful parametrization allows for a reliable extrapolation to the lowest energies where the measured spectrum is affected by the detection thresholds which are not adequately known.

We adopt a parametrization similar to one used in previous studies [19,20,50,52] based on the R-matrix single-channel approximation [53]. The decay is assumed to proceed by allowed transitions to the three known, energetically accessible 2^+ states in ^{8}Be: the first excited state at 3 MeV and the two strongly isospin-mixed states at 16.626 and 16.922 MeV. A satisfactory description of the E_x distribution is, however, only achieved with the inclusion of a fourth 2^+ state above the β-decay window.

Each state, λ, is characterized by an excitation energy, $\mathcal{E}_\lambda$, a reduced width amplitude, γ_λ, and two β-decay strength parameters, $g_{\mathrm{F},\lambda}$ and $g_{\mathrm{GT},\lambda}$, giving the Fermi and Gamow-Teller strength, respectively. We label the states in order of increasing energy. In the standard R-matrix formalism used in previous studies, the E_x distribution is given by

$$\mathcal{F}(E_x) = \frac{Nt_{1/2}}{\pi B} f_\beta(E_x) P_\ell(E_x) \times \frac{\left|\sum_\lambda \frac{g_{\mathrm{F},\lambda}\gamma_\lambda}{\mathcal{E}_\lambda - E_x}\right|^2 + \left|\sum_\lambda \frac{g_{\mathrm{GT},\lambda}\gamma_\lambda}{\mathcal{E}_\lambda - E_x}\right|^2}{\left|1 - [S_\ell(E_x) - B_\ell + iP_\ell(E_x)]\sum_\lambda \frac{\gamma_\lambda^2}{\mathcal{E}_\lambda - E}\right|^2}, \quad (10)$$

where N is the number of β decays, $t_{1/2} = 770(3)$ ms is the half-life of ^{8}B [12], and $B = 6147(2)$ s [54]. $f_\beta(E_x)$ is the integrated phase space available to the leptons, here evaluated according to the parametrization of Ref. [51]. $P_\ell(E_x)$ and $S_\ell(E_x)$ are the penetration and shift functions, respectively, $\ell = 2$ being the orbital angular momentum of the two α particles. Finally, B_ℓ is the boundary condition parameter. In the previous studies [19,20,50,52], $B_\ell = S_\ell(\mathcal{E}_1)$ was used, which ensures that the R-matrix parameters of the 3-MeV state coincide with the "observable" resonance parameters.

In the present study we rely on the alternative R-matrix formalism of Ref. [55] in which the standard R-matrix parameters, $\mathcal{E}_\lambda, \gamma_\lambda, g_{\mathrm{F},\lambda}, g_{\mathrm{GT},\lambda}$, are replaced by the "observable" resonance parameters, $\widetilde{\mathcal{E}}_\lambda, \widetilde{\gamma}_\lambda, \widetilde{g}_{\mathrm{F},\lambda}, \widetilde{g}_{\mathrm{GT},\lambda}$. The advantage of the alternative formalism is that it allows the energies and reduced widths of an arbitrary number of states to be easily fixed in the fitting procedure. We stress that the alternative formalism is mathematically equivalent to the standard R-matrix formalism used in the previous studies. The alternative parameters may be converted to the standard R-matrix parameters by a straightforward matrix diagonalization procedure described in Ref. [55]. In the alternative formalism, the E_x distribution is given by

$$\mathcal{F}(E_x) = \frac{Nt_{1/2}}{\pi B} f_\beta(E_x) P_\ell(E_x) \times \left\{\left|\sum_{\lambda\mu} \widetilde{g}_{\mathrm{F},\lambda}\widetilde{\gamma}_\mu \widetilde{A}_{\lambda\mu}\right|^2 + \left|\sum_{\lambda\mu} \widetilde{g}_{\mathrm{GT},\lambda}\widetilde{\gamma}_\mu \widetilde{A}_{\lambda\mu}\right|^2\right\}, \quad (11)$$

where $\widetilde{\boldsymbol{A}}$ is the level matrix of the alternative formalism, defined by its inverse,

$$(\widetilde{\boldsymbol{A}}^{-1})_{\lambda\mu} = (\widetilde{\mathcal{E}}_\lambda - E_x)\delta_{\lambda\mu} - \widetilde{\gamma}_\lambda\widetilde{\gamma}_\mu[\,S_\ell(E_x) + iP_\ell(E_x)\,] + \begin{cases} \widetilde{\gamma}_\lambda^2 \mathcal{S}_\lambda, & \lambda = \mu, \\ \widetilde{\gamma}_\lambda\widetilde{\gamma}_\mu \frac{\mathcal{S}_\lambda(E_x - \widetilde{\mathcal{E}}_\mu) - \mathcal{S}_\mu(E_x - \widetilde{\mathcal{E}}_\lambda)}{\widetilde{\mathcal{E}}_\lambda - \widetilde{\mathcal{E}}_\mu}, & \lambda \neq \mu, \end{cases} \quad (12)$$

where $\delta_{\lambda\mu}$ is the Kronecker's δ and $\mathcal{S}_\lambda = S_\ell(\widetilde{\mathcal{E}}_\lambda)$. Instead of the β-decay strength parameters, $\widetilde{g}_{\mathrm{F},\lambda}$ and $\widetilde{g}_{\mathrm{GT},\lambda}$, one often quotes the corresponding matrix elements, $M_{\mathrm{F},\lambda}$ and $M_{\mathrm{GT},\lambda}$, which are related to the strength parameters as

$$M_{\mathrm{X},\lambda} = \frac{\widetilde{g}_{\mathrm{X},\lambda}}{\left(1 + \widetilde{\gamma}_\lambda^2 \frac{dS_\ell}{dE_x}|_{E_x=\widetilde{E}_\lambda}\right)^{1/2}}, \quad (13)$$

where $\mathrm{X} = \mathrm{F}, \mathrm{GT}$. With this definition, the reduced transition strengths are given by $B_{\mathrm{X},\lambda} = (g_A/g_V)^{-2}|M_{X,\lambda}|^2$, where $|g_A/g_V| = 1.2695(29)$ [56]. Note that the present definition of the matrix elements differs slightly from the definition used in Refs. [19,20,50,52], where, simply, $M_{\mathrm{X},\lambda} = g_{\mathrm{X},\lambda}$.

The energy, the reduced width, and the Gamow-Teller strength of the 3-MeV state are considered free parameters. Measurements of the β-ν-α correlation in the decays of ^{8}Li and ^{8}B indicate a negligible Fermi component in the energy region $2 < E_x < 8$ MeV [57] in agreement with shell-model calculations [58]. Accordingly, we fix the Fermi strength of the 3-MeV state to zero.

Following Refs. [59,60], the 16.626- and 16.922-MeV states are written as linear combinations of the $T = 1$ isospin analog of the ^{8}Li and ^{8}B ground states and a $T = 0$ component. The Fermi strength to the $T = 0$ component is zero. The Fermi strength to the $T = 1$ component is that of a superallowed transition, that is, $|M_{\mathrm{F}}| = \sqrt{2}$. The Gamow-Teller strength to the $T = 0$ component is considered a free parameter. As discussed in Ref. [52], shell-model calculations predict a negligible Gamow-Teller strength to the $T = 1$ component. Accordingly, we fix it to zero. We fix the level energies and reduced widths to the values determined from $\alpha + \alpha$ elastic scattering data [61]. In doing so, we perform the necessary corrections for the interference with other 2^+ states, as pointed out in Ref. [60] but overlooked in the previous studies of Refs. [19,20,50,52].

In contrast to Refs. [19,20,50,52], which used a fixed energy of 37 MeV for the fourth 2^+ state, we shall allow its energy to vary. The reduced width and the Gamow-Teller strength are also considered free parameters while the Fermi strength is fixed to zero.

The channel radius is fixed to $a = 4.5$ fm. A detailed account of the present parametrization is given in Ref. [62].

B. Fitting and uncertainties

In Fig. 22, the experimental data have been fitted above 1.5 MeV using Eq. (11) folded with the response function given by Eq. (6). As discussed in Sec. III F, the single-α detection efficiency could not be determined reliably below $E_\alpha \approx 0.7$ MeV. For this reason, we do not include data below 1.5 MeV in the fit. The fit gives an excellent description of the

TABLE I. Best-fit parameter values. Energies are in MeV. $\theta_\lambda = \widetilde{\gamma}_\lambda/\gamma_W$ is the reduced width in units of the Wigner limit, $\gamma_W^2 = \hbar^2/ma^2 = 1.028$ MeV, where $m = \frac{1}{2}m_\alpha$ is the reduced mass and $a = 4.5$ fm is the channel radius. The statistical uncertainty is given first followed by the systematic uncertainty owing to the uncertainty on the energy scale. The energies and reduced widths of the 16.626- and 16.922-MeV states were fixed as described in Ref. [62], hence the zero statistical uncertainties.

Parameter	Value
$\widetilde{\mathcal{E}}_1$	$3.019 \pm 0.003 \pm 0.003$
θ_1	$1.008 \pm 0.003 \pm 0.004$
$M_{GT,1}$	$-0.1248 \pm 0.0004 \pm 0.0001$
$\widetilde{\mathcal{E}}_2$	$16.530 \pm 0 \pm 0.005$
θ_2	$0.207 \pm 0 \pm 0.01$
$\widetilde{\mathcal{E}}_3$	$16.883 \pm 0 \pm 0.002$
θ_3	$0.113 \pm 0 \pm 0.002$
$M_{GT,23}$	$1.82 \pm 0.02 \pm 0.01$
$\widetilde{\mathcal{E}}_4$	$29.8 \pm 1.4 \pm 0.8$
θ_4	$2.23 \pm 0.05 \pm 0.03$
$M_{GT,4}$	$-0.24 \pm 0.03 \pm 0.01$

data with $\chi^2/\mathrm{DOF} = 0.93$, where DOF stands for degrees of freedom. The best-fit parameter values are given in Table I.

The E_x distribution obtained from the fit is available online in table format [63]. The 1σ statistical and systematic uncertainties on the E_x distribution are shown in Fig. 23. The

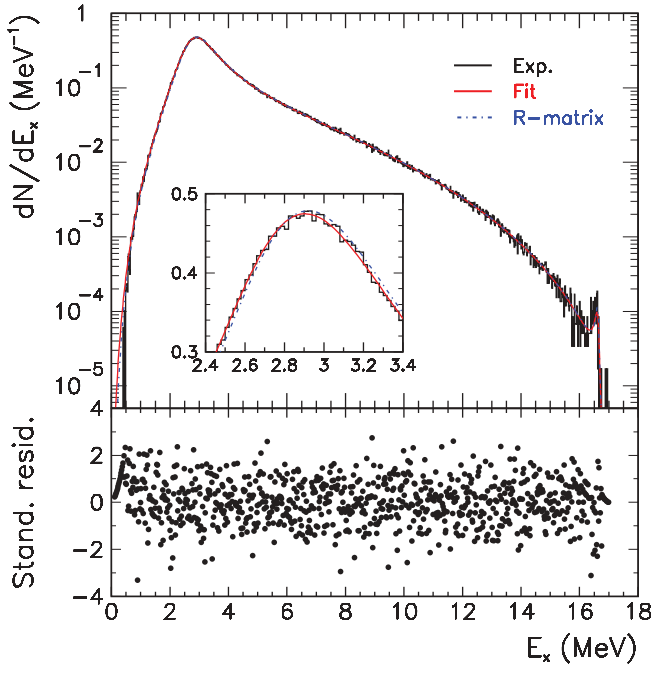

FIG. 22. (Color online) The histogram shows the experimental data. The solid curve (red) shows the best fit using Eq. (11) folded with Eq. (6). The dash-dotted curve (blue) shows Eq. (11) without folding. The inset shows a magnification of the peak region. The 19-keV shift owing to the response function is hardly visible. The standardized residuals for the best fit are shown at the bottom.

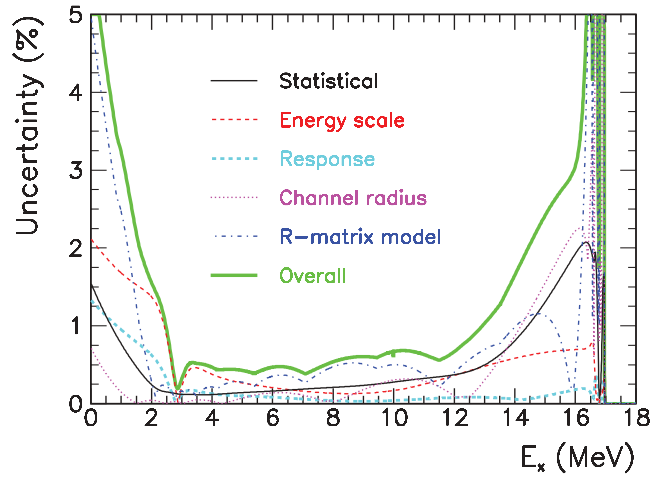

FIG. 23. (Color online) 1σ statistical and systematic uncertainties on the E_x distribution, $\mathcal{F}(E_x)$, in percent of the distribution value. The large fluctuations around 16–17 MeV are attributable to the presence of the narrow 16.626- and 16.922-MeV states.

overall uncertainty has been obtained by adding the individual uncertainties in quadrature. The statistical uncertainties were obtained by standard error propagation of the full covariance matrix of the fit parameters.

The systematic uncertainty owing to the uncertainty on the energy scale, $\sigma_x(E_x)$, shown in Fig. 21, was estimated by rebinning the experimental spectrum with a high and a low calibration, differing from the central calibration by $\pm\sigma_x(E_x)$, respectively. New R-matrix fits were made to these spectra yielding distributions $\mathcal{F}_\pm(E_x)$ with $\chi^2/\mathrm{DOF} = 0.99$ and 1.03, respectively. Finally, the deviations $|\mathcal{F}_\pm(E_x) - \mathcal{F}(E_x)|$ were calculated and the larger of the two adopted as the (symmetric) energy-scale uncertainty on $\mathcal{F}(E_x)$.

The systematic uncertainty owing to the uncertainty on the response function was estimated by performing fits with the amplitude of the satellite peak, g, fixed to 3.5% and 4.5%, instead of the standard 4.0%, yielding distributions $\mathcal{F}_{g\pm}(E_x)$ with $\chi^2/\mathrm{DOF} = 0.94$ in both cases. The deviations $|\mathcal{F}_{g\pm}(E_x) - \mathcal{F}(E_x)|$ were calculated and the larger of the two adopted as the (symmetric) response-function uncertainty on $\mathcal{F}(E_x)$.

The choice of channel radius in the R-matrix model represents a source of systematic uncertainty outside the fit region which we estimate by performing fits with low and high choices of channel radius ($a = 4.0$ and 5.0 fm), yielding distributions $\mathcal{F}_{a\pm}(E_x)$ with $\chi^2/\mathrm{DOF} = 0.94$ in both cases. We calculate the deviations $|\mathcal{F}_{a\pm}(E_x) - \mathcal{F}(E_x)|$ and adopt the larger of the two as the (symmetric) channel-radius uncertainty on $\mathcal{F}(E_x)$.

The invocation of a fourth 2^+ state above the β-decay window to reproduce the decay strength not accounted for by the three known 2^+ states, represents an additional source of uncertainty not recognized in previous studies. To quantify the uncertainties associated with the choice of model, we perform fits using two alternative models giving equally good fits to the data ($\chi^2/\mathrm{DOF} = 0.94$ obtained in both cases): one in which

the energy of the fourth 2^+ state is fixed to 37 MeV, as was done in previous studies, and one in which the fourth 2^+ state is placed *inside* the β-decay window with the energy determined by the fit. In the latter case, a larger channel radius of 6.7 fm was required to achieve a satisfactory fit, consistent with Ref. [60], where this model was used. We calculate the deviation relative to $\mathcal{F}(E_x)$ for both models and adopt the larger of the two as the (symmetric) model uncertainty on $\mathcal{F}(E_x)$. As Fig. 23 shows, the model uncertainty dominates outside the fit region ($E_x < 1.5$ MeV).

C. Comparison to previous studies

In Fig. 24, we compare the E_x distribution obtained in the present study to the distributions obtained in the studies at Notre Dame [18], at Argonne [19], and in Seattle [20]. As the present distribution, the Argonne and Seattle distributions represent R-matrix fits to data, whereas the Notre Dame distribution represents actual (efficiency corrected) data. The widths of the curves and the error bars on the data points show 1σ uncertainties, in all cases obtained by adding statistical and systematical uncertainties in quadrature. The two systematic uncertainties quoted on the Seattle distribution were added in quadrature as recommended. The Argonne and Seattle distributions are published in table format. The Notre Dame distribution was made available to us by A. Garcia. The maximum of the present distribution lies between the maximum of the Notre Dame distribution and the maxima of the Argonne and Seattle distributions, which are very close. The precise location of the maxima are given in Table II and shown graphically in Fig. 25.

Relative deviations of the Argonne and Seattle distributions compared to the present distribution, are shown in Fig. 26.

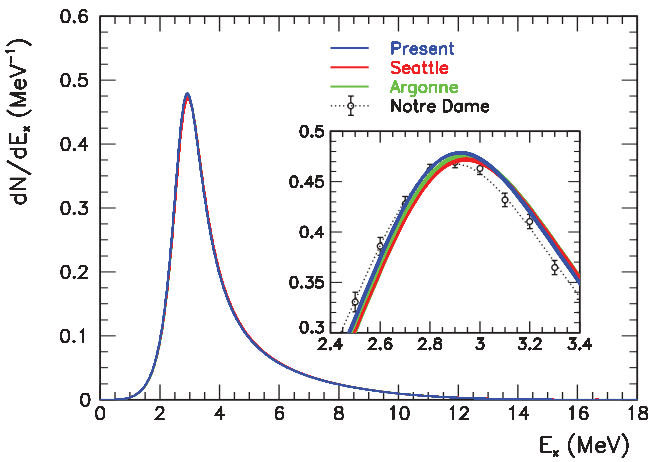

FIG. 24. (Color online) Comparison of the E_x distribution obtained in the present study to the distributions obtained in the previous studies at Notre Dame [18], at Argonne [19], and in Seattle [20]. The Argonne and Seattle distributions practically lie on top of each other. The widths of the curves and the error bars on the data points show 1σ uncertainties. The dashed line going through the Notre dame data points is merely meant to guide the eye. All four distributions have been normalized to unit area.

TABLE II. Spectral maxima of the E_x distributions obtained in the present and previous three studies.

Study	Spectral maximum (keV)	Deviation from present study (keV)	1σ uncertainty at maximum (keV)
Notre Dame [18]	2899	−22	12
Argonne [19]	2943	22	9
Seattle [20]	2939	18	5
Present	2921	0	5

The gray band shows the overall 1σ uncertainty on the present distribution. For clarity, the uncertainties on the Argonne and Seattle distributions are not shown. The large fluctuations at the extremes are attributable to the limited precision of the published tables on the Argonne and Seattle distributions, as well as the presence of the narrow 16.626- and 16.922-MeV states. The Argonne and Seattle distributions can be brought in reasonable agreement with the present distribution by shifting them down in energy by 22 and 18 keV, respectively, such that the spectral maxima coincide. Even so, deviations remain, in particular below 2 MeV. The relative deviation of the shifted Seattle distribution with respect to the present distribution exhibits a dip at 2.9 MeV. This shows that the peak of the Seattle distribution is slightly wider, suggesting that experimental broadening effects have not been completely accounted for in the analysis of the Seattle data. As discussed in Sec. V B, three reliable spectra (I,II,IV) were extracted from the present measurement, two of which (I,II) overlap in data content. Spectrum II was selected as the preferred spectrum. The curves labeled "Present I" and "Present IV" show the relative deviations of R-matrix fits to spectra I and IV compared to the R-matrix fit to spectrum II. The fits are generally in good agreement though spectrum IV exhibits somewhat large deviations around 12 MeV.

Starting with the Notre Dame measurement, we are unable to explain the 22-keV discrepancy with respect to the present measurement (Fig. 25). We may note, however, that because the Notre Dame measurement, like the present measurement,

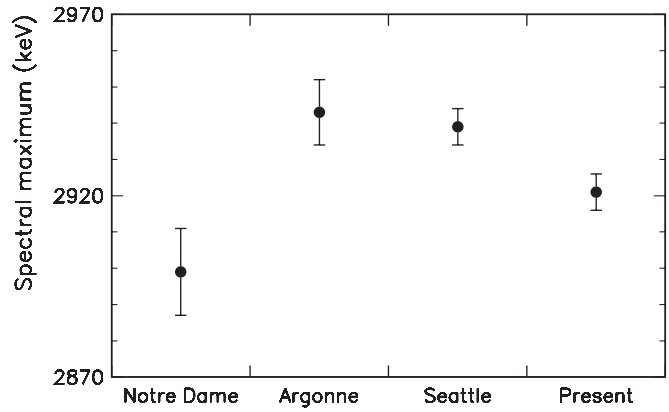

FIG. 25. Spectral maxima of the E_x distributions obtained in the present and previous three studies.

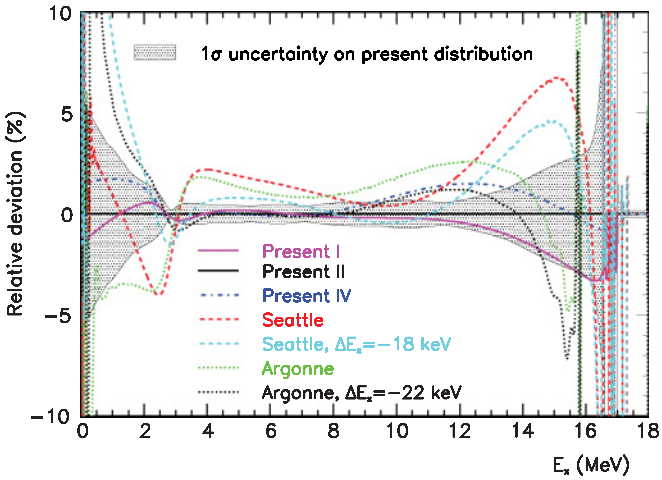

FIG. 26. (Color online) Relative deviations of the Argonne and Seattle distributions compared to the present distribution. The gray band shows the overall 1σ uncertainty on the present distribution. The large fluctuations at the extremes are attributable to the limited precision of the published tables on the Argonne and Seattle distributions as well as the presence of the narrow 16.626- and 16.922-MeV states. The curves labeled "Present I" and "Present IV" show the relative deviations of R-matrix fits to spectra I and IV compared to the R-matrix fit to spectrum II.

relies on the determination of individual α energies, an error of 10 keV in the energy calibration is enough to explain the discrepancy. As already mentioned, it was recently reported [21] that the members of the Notre Dame collaboration now recognize that they underestimated uncertainties related to the energy loss generated by the carbon buildup in their catcher foil. Considering that the largest energy-loss correction made in the analysis of the Notre Dame data was 25 keV (at $E_\alpha = 0.5$ MeV), it seems unlikely that the energy loss should have been underestimated by as much as 20–25 keV (the amount needed to obtain agreement with the Argonne and Seattle measurements).

Turning to the Argonne measurement, we have identified two sources of systematic uncertainty in the energy calibration. First, the calibration relies on the measurement of the linearly added signals from the ^{20}Na decay products, that is, $\alpha + {}^{16}$O. We suspect that the different response of the Si detector to α particles and ^{16}O ions was not accounted for correctly. TRIM simulations were used to determine the amount of energy lost by the ^{16}O ions through nonionizing processes, but, as argued in Sec. III E, TRIM could be wrong by 5–10 keV. Second, an external ^{228}Th α source was used to provide calibration points at higher energies (5–9 MeV). Corrections were made for the energy loss of the α particles in the source, but it is unclear whether the different implantation depth of the α emitters in the decay chain of ^{228}Th was taken into account. As discussed in Sec. III D, this effect may have distorted the energy calibration.

Finally, we suspect that an overestimation of the exponential tails associated with the detector response may explain the Seattle result. In the Seattle measurement, a standard ^{148}Gd α source was used to determine the response function which was then folded into the R-matrix fit. The effect of the exponential tails is to shift the extracted E_x distribution up in energy. In the present study, we find that the response function determined from the α-source data has considerably stronger exponential tails than the response function determined from the ^{20}Na data, a difference that may be attributed to energy-loss effects in the α-source material (Sec. III G). The α-source measurement made in Seattle could have been subject to similar effects.

D. Consequences for the neutrino spectrum

The calculation of the neutrino energy spectrum from the E_x distribution is complicated by the presence of recoil terms, affecting the neutrino spectrum at the level of 5%–10%. In addition, radiative corrections affect the neutrino spectrum at the level of 1%. A detailed and comprehensive account of the steps involved in the calculation and an estimate of the associated theoretical uncertainties is given in Ref. [19]. Here we limit ourselves to a simpler calculation, the purpose being to estimate how the neutrino spectrum is modified by our—what we believe to be—improved determination of the E_x distribution. A complete calculation, following the prescription of Ref. [19], will be published separately.

Neglecting recoil terms and radiative corrections, the positron energy spectrum, for fixed excitation energy, E_x, is given by

$$\frac{dN}{dE_\beta} \propto p_\beta E_\beta (E_0 - E_x - E_\beta)^2 F(-Z, E_\beta), \qquad (14)$$

where p_β and E_β are the positron momentum and total energy, $E_0 = 17.4688(10)$ MeV is the maximum total positron energy for decays to the ground state of ^{8}Be, and $F(-Z, E_\beta)$ is the Fermi function which describes the modification of the β phase space by the Coulomb interaction between the positron and the daughter nucleus of charge Z. We evaluate $F(-Z, E_\beta)$ using the analytical expression given in Ref. [64] which includes relativistic corrections but does not account for the screening of the nuclear Coulomb field by the atomic electrons. The positron spectrum is calculated by integrating Eq. (14) over all excitation energies, E_x, weighted by the E_x distribution, $\mathcal{F}(E_x)$. The neutrino spectrum is obtained by the simple substitution $E_\nu = E_0 - E_x - E_\beta$.

Following this simplified procedure, we calculate two neutrino spectra: one using the E_x distribution obtained in the present study and one using the Argonne E_x distribution. The neutrino spectrum calculated using the E_x distribution obtained in the present study is shown in Fig. 27(a). The 1σ statistical and systematic uncertainties on the present neutrino spectrum are shown in Fig. 27(b). Finally, the relative deviation with respect to the spectrum obtained using the Argonne E_x distribution is shown in Fig. 27(c).

A significant deviation of several percent is seen at high neutrino energies with the present spectrum at these energies being the most intense. The odd-looking wiggle around 0.5 MeV is attributable to a slight shift in the positions of the 16.626- and 16.922-MeV peaks. The larger intensity of the present neutrino spectrum in the 11-to-14-MeV region is a natural consequence of the 3-MeV peak of the present E_x

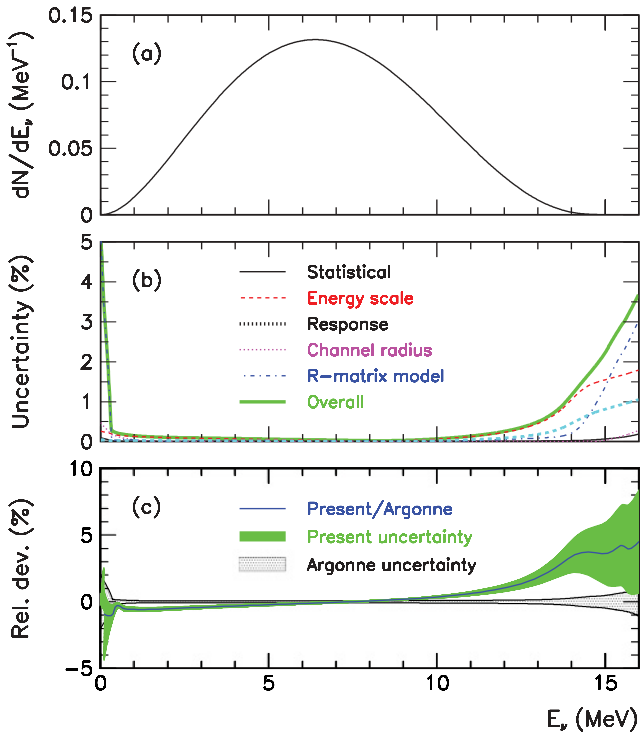

FIG. 27. (Color online) (a) Neutrino spectrum calculated using the E_x distribution obtained in the present study neglecting recoil terms and radiative corrections. Note that the end point of the neutrino spectrum (16.96 MeV) is slightly outside the energy range chosen for the plot owing to insufficient numerical precision above 16 MeV. (b) 1σ statistical and systematic uncertainties on the present neutrino spectrum. (c) Relative deviation with respect to the neutrino spectrum calculated using the Argonne E_x distribution.

distribution being shifted 22 keV down in energy compared to the Argonne distribution. Above ∼14 MeV the shape of the neutrino spectrum is determined by the low-energy flank of the 3-MeV peak. The large uncertainty on the neutrino spectrum above ∼14 MeV reflects the uncertainty associated with the extrapolation of the E_x distribution to energies below $E_x < 1.5$, where the fit is not constrained by the experimental data.

E. Results not related to the neutrino spectrum

The β-delayed 2α breakup of the 16.922-MeV state in ^{8}Be, situated only 36 keV below the end point of the β-decay window, has been observed for the first time. Five events were detected from the 16.922-MeV state compared to 180 events from the 16.626-MeV state. Assuming that the β-decay matrix elements to the 16.922- and 16.626-MeV states are the same, their relative feeding is determined by the available phase space. Electron capture (EC) dominates over β decay for the 16.922-MeV state (EC/$\beta = 75$) owing to its proximity to the end point of the β-decay window. In contrast, β decay dominates for the 16.626-MeV state (EC/$\beta = 0.04$). We calculate the relative feeding to be 2.4×10^{-2}, in good agreement with the observed ratio of $5/180 = 3 \times 10^{-2}$.

VII. SUMMARY AND CONCLUSION

Accurate knowledge of the ^{8}B neutrino spectrum is of great importance to the interpretation of the solar neutrino measurements. Experimentally, the ^{8}B neutrino spectrum is determined from the measurement of the distribution of excitation energies populated in the daughter nucleus, ^{8}Be.

Our collaboration has performed two independent measurements of the ^{8}B neutrino spectrum using different experimental techniques. Here we have presented the results of the first measurement, performed at the IGISOL facility in Jyväskylä, Finland, using a coincidence technique similar to that used at Notre Dame [18]. The α particles were detected in coincidence in separate detectors facing a thin carbon foil in which the ^{8}B activity was implanted at 20 keV. Our setup differs from the Notre Dame setup in that segmented Si detectors were used to reduce β summing and unwanted background from β-α coincidences. Consequently, a strong magnetic field to sweep away the positrons was not needed. This was a significant source of systematic uncertainty in the Notre Dame measurement. The β-delayed α emitter ^{20}Na was used for energy calibration as it was in the Argonne measurement [19]. By implanting the ^{20}Na activity in the same foil as used for the ^{8}B activity, the systematic uncertainty from energy loss corrections is reduced compared to the Notre Dame and the Seattle [20] measurements where standard α sources were used for the energy calibration. The energies of the α particle and the recoiling ^{16}O ion were measured separately, making it unnecessary to correct for the different response of Si detectors to α particles and ^{16}O ions as was required for the Argonne measurement.

The excitation energy distribution obtained in the present study is shifted 20 keV down in energy relative to the internally consistent distributions obtained at Argonne and in Seattle, which are held as the current standard [21]. The present distribution results in a more intense neutrino spectrum at high energies. The deviation reaches 4% at 16 MeV. Below 11 MeV, the present neutrino spectrum deviates by less than 1% from the Argonne neutrino spectrum. We believe that our experimental approach gives an improved handle on systematical effects compared to the approaches adopted at Argonne and in Seattle. We have pointed out uncertainties in their measurements which may explain the 20-keV shift. As an important improvement over previous studies, we fit the data with different R-matrix models, resulting in a more truthful estimate of the systematical uncertainty associated with the extrapolation to excitation energies below the fit region.

The complete calculation of the neutrino spectrum following the prescription of Ref. [19] is under way and will be published in a separate paper. However, the conclusions already made regarding the implications of our new measurement for the neutrino spectrum will not change substantially. The deviation relative to the Argonne neutrino spectrum is well below the precision of the existing solar neutrino data except at the very highest neutrino energies ($E_\nu > 13$ MeV), where the deviation may have some implication, in particular for the upper limit on the *hep* neutrino signal [10].

The results from the second measurement performed by our collaboration at KVI in Groningen, The Netherlands,

will provide an important check of the present results and is expected to provide a more reliable determination of the low-energy part of the excitation energy distribution which, in turn, should help to reduce the systematic uncertainties on the high-energy part of the neutrino spectrum.

ACKNOWLEDGMENTS

This work has been supported by the EU 6th Framework Programme "Integrating Infrastructure Initiative—Transnational Access," Contract No. 506065 (EURONS, JRAs TRAPSPEC and DLEP), by the Academy of Finland under the Finnish Centre of Excellence Programme 2006-2011 (Project No. 213503, Nuclear and Accelerator Based Physics Programme at JYFL), by the Nordic Infrastructure Project (NordForsk Project No. 070315), and by the Spanish Funding Agency MICINN (Contract No. FPA2009-07387). O.S.K. acknowledges the support from the Villum Kann Rasmussen Foundation, and A.S. acknowledges the support from the Jenny and Antti Wihuri Foundation. We thank the crew of the K130 cyclotron in Jyväskylä for excellent operation.

[1] J. N. Bahcall, A. M. Serenelli, and S. Basu, Astrophys. J. **621**, L85 (2005).
[2] L. Wolfenstein, Phys. Rev. D **17**, 2369 (1978).
[3] S. P. Mikheyev and A. Y. Smirnov, Sov. J. Nucl. Phys. **42**, 913 (1985).
[4] H. A. Bethe, Phys. Rev. Lett. **56**, 1305 (1986).
[5] Q. R. Ahmad *et al.* (SNO Collaboration), Phys. Rev. Lett. **87**, 071301 (2001); (SNO Collaboration), **89**, 011301 (2002).
[6] J. N. Bahcall, P. I. Krastev, and A. Y. Smirnov, Phys. Rev. D **60**, 093001 (1999).
[7] J. P. Cravens *et al.* (SK Collaboration), Phys. Rev. D **78**, 032002 (2008).
[8] B. Aharmim *et al.* (SNO Collaboration), Phys. Rev. C **81**, 055504 (2010).
[9] M. B. Smy *et al.* (SK Collaboration), J. Phys. Conf. Ser. **203**, 012082 (2010).
[10] B. Aharmim *et al.* (SNO Collaboration), Astrophys J. **653**, 1545 (2006).
[11] G. Bellini *et al.* (Borexino Collaboration), Phys. Rev. D **82**, 033006 (2010).
[12] D. R. Tilley *et al.*, Nucl. Phys. A **745**, 155 (2004).
[13] M. K. Bacrania, N. M. Boyd, R. G. H. Robertson, and D. W. Storm, Phys. Rev. C **76**, 055806 (2007).
[14] B. J. Farmer and C. M. Class, Nucl. Phys. **15**, 626 (1960).
[15] D. H. Wilkinson and D. E. Alburger, Phys. Rev. Lett. **26**, 1127 (1971).
[16] L. De Braeckeleer and D. Wright (unpublished); L. De Braeckeleer *et al.*, Phys. Rev. C **51**, 2778 (1995).
[17] J. Napolitano, S. J. Freedman, and J. Camp, Phys. Rev. C **36**, 298 (1987).
[18] C. E. Ortiz, A. García, R. A. Waltz, M. Bhattacharya, and A. K. Komives, Phys. Rev. Lett. **85**, 2909 (2000).
[19] W. T. Winter *et al.*, Phys. Rev. Lett. **91**, 252501 (2003); W. T. Winter, S. J. Freedman, K. E. Rehm, and J. P. Schiffer, Phys. Rev. C **73**, 025503 (2006).
[20] M. Bhattacharya, E. G. Adelberger, and H. E. Swanson, Phys. Rev. C **73**, 055802 (2006).
[21] E. G. Adelberger *et al.*, Rev. Mod. Phys. **83**, 195 (2010).
[22] T. Roger *et al.* (unpublished).
[23] J. Äystö, Nucl. Phys. A **693**, 477 (2001).
[24] J. Huikari *et al.*, Nucl. Instr. Meth. B **222**, 632 (2004).
[25] P. Karvonen *et al.*, Nucl. Instrum. Methods Phys. Res., Sect. B **266**, 4794 (2008).
[26] C. R. McClenahan *et al.*, Phys. Rev. C **11**, 370 (1975).
[27] K. E. Sale *et al.*, Phys. Rev. C **41**, 2418 (1990).
[28] K. Peräjärvi *et al.*, Phys. Lett. B **492**, 1 (2000).
[29] O. Tengblad *et al.*, Nucl. Instrum. Methods Phys. Res., Sect. A **525**, 458 (2004).
[30] K. Yu, C. W. Y. Yip, D. Nikezic, J. P. Y. Ho, and V. S. Y. Koo, App. Rad. Isot. **59**, 363 (2003).
[31] D. R. Tilley, C. M. Cheves, J. H. Kelley, S. Raman, and H. R. Weller, Nucl. Phys. A **636**, 249 (1998).
[32] J. F. Ziegler, SRIM/TRIM [http://srim.org/].
[33] R. B. Firestone and V. S. Shirley, *Table of Isotopes*, 8th ed. (Wiley & Sons, New York, 1996).
[34] R. A. Gough, R. G. Sextro, and J. Cerny, Phys. Rev. Lett. **28**, 510 (1972).
[35] R. J. Tighe, J. C. Batchelder, D. M. Moltz, T. J. Ognibene, M. W. Rowe, J. Cerny, and B. A. Brown, Phys. Rev. C **52**, R2298 (1995).
[36] F. Stegmüller, C. Rolfs, S. Schmidt, W. H. Schulte, H. P. Trautvetter, and R. W. Kavanagh, Nucl. Phys. A **601**, 168 (1996).
[37] A. L. Sallaska *et al.*, Phys. Rev. Lett. **105**, 152501 (2010).
[38] R. B. Firestone, Nucl. Data Sheets **108**, 1 (2007).
[39] W. N. Lennard, H. Geissel, K. B. Winterbon, D. Phillips, T. K. Alexander, and J. S. Forster, Nucl. Instr. Meth. A **248**, 454 (1986).
[40] W. N. Lennard and K. B. Winterbon, Nucl. Instr. Meth. B **24**, 1035 (1987).
[41] O. S. Kirsebom *et al.* (unpublished).
[42] E. T. H. Clifford *et al.*, Nucl. Phys. A **493**, 293 (1989).
[43] O. S. Kirsebom *et al.* (unpublished).
[44] H. Paul, Nucl. Instr. Meth. B **268**, 3421 (2010).
[45] N. P. Barradas, E. Alves, Z. Siketić, I. Bogdanović Radović, AIP Conf. Proc. **1099**, 331 (2009).
[46] L. Buchmann *et al.*, Phys. Rev. C **75**, 012804(R) (2007).
[47] D. R. Tilley, H. R. Weller, C. M. Cheves, and R. M. Chasteler, Nucl. Phys. A **595**, 1 (1995).
[48] K. I. Hahn, C. R. Brune, and P. R. Wrean, Phys. Rev. C **48**, 914 (1993).
[49] J. Yorkston, A. C. Shotter, D. B. Syme, and G. Huxtable, Nucl. Instr. Meth. A **262**, 353 (1987).
[50] M. Bhattacharya and E. G. Adelberger, Phys. Rev. C **65**, 055502 (2002).
[51] D. H. Wilkinson and B. E. F. Macefield, Nucl. Phys. A **232**, 58 (1974).
[52] E. K. Warburton, Phys. Rev. C **33**, 303 (1986).
[53] A. M. Lane and R. G. Thomas, Rev. Mod. Phys. **30**, 257 (1958).
[54] J. C. Hardy and I. S. Towner, Phys. Rev. C **71**, 055501 (2005).
[55] C. R. Brune, Phys. Rev. C **66**, 044611 (2002).

[56] W.-M. Yao *et al.*, J. Phys. G: Nucl. Part. Phys. **33**, 1 (2006).
[57] R. D. McKeown, G. T. Garvey, and C. A. Gagliardi, Phys. Rev. C **22**, 738 (1980); **26**, 2336 (1982).
[58] F. C. Barker, Nucl. Phys. **83**, 418 (1966).
[59] F. C. Barker, Aust. J. Phys. **22**, 293 (1969).
[60] F. C. Barker, Aust. J. Phys. **42**, 25 (1989).
[61] F. Hinterberger *et al.*, Nucl. Phys. A **229**, 397 (1978).
[62] S. Hyldegaard, Ph.D. thesis, Aarhus University, 2010 [http://phys.au.dk/fileadmin/site_files/publikationer/phd/Solveig_Hyldegaard.pdf].
[63] See supplemental material at [http://link.aps.org/supplemental/10.1103/PhysRevC.83.065802] for a table containing the present E_x distribution.
[64] J. M. Blatt and V. F. Weisskopf, *Theoretical Nuclear Physics* (Wiley & Sons, New York, 1952).